

MILKY WAY RED DWARFS IN THE BORG SURVEY;  
GALACTIC SCALE-HEIGHT AND THE DISTRIBUTION OF DWARFS STARS IN WFC3 IMAGING

B. W. HOLWERDA<sup>1,2</sup>, M. TRENTI<sup>3</sup>, W. CLARKSON<sup>4</sup>, K. SAHU<sup>5</sup>, L. BRADLEY<sup>5</sup>, M. STIAVELLI<sup>5</sup>, N. PIRZKAL<sup>5</sup>,  
G. DE MARCHI<sup>2</sup>, M. ANDERSEN<sup>6</sup>, R. BOUWENS<sup>1</sup>, R. RYAN<sup>5</sup>

*ApJ* in prep

ABSTRACT

We present a tally of Milky Way late-type dwarf stars in 68 WFC3 pure-parallel fields (227 arcmin<sup>2</sup>) from the Brightest of Reionizing Galaxies (BoRG) survey for high-redshift galaxies. Using spectroscopically identified M-dwarfs in two public surveys, the CANDELS and the ERS mosaics, we identify a morphological selection criterion using the half-light radius ( $r_{50}$ ), a near-infrared J-H, G-J color region where M-dwarfs are found, and a V-J relation with M-dwarf subtype.

We apply this morphological selection of stellar objects, color-color selection of M-dwarfs and optical-near-infrared color subtyping to compile a catalog of 274 M-dwarfs belonging to the disk of the Milky Way with a limiting magnitude of  $m_{F125W} < 24(AB)$ . Based on the M-dwarfs statistics, we conclude that (a) the previously identified North/South discrepancy in M-dwarf numbers persists in our sample; there are more M-dwarfs in the Northern fields on average than in Southern ones, (b) the Milky Way's single disk scale-height for M-dwarfs is 0.3-4 kpc, depending on sub-type, (c) the scale-height depends on M-dwarf subtype with early type (M0-4) high scale-height ( $z_0 = 3 - 4$  kpc) and later types M5 and above in the thin disk ( $z_0 = 0.3 - 0.5$  kpc). (d) a second component is visible in the vertical distribution, with a different, much higher scale-height in the Southern Fields compared to the Northern ones. We report the M-dwarf component of the Sagittarius stream in one of our fields with 11 confirmed M-dwarfs, 7 of which are at the stream's distance. In addition to the M-dwarf catalog, we report the discovery of 1 T-dwarf and 30 L-dwarfs from their near-infrared colors. The dwarf scale-height and the relative low incidence in our fields of L- and T-dwarfs in these fields makes it unlikely that these stars will be interlopers in great numbers in color-selected samples of high-redshift galaxies. The relative ubiquity of M-dwarfs however will make them ideal tracers of Galactic Halo substructure with EUCLID and reference stars for JWST observations.

1. INTRODUCTION

Counting stars to infer the shape and size of our Milky Way Galaxy is a classic experiment in Astronomy. However, it is also among the most prone to insufficient data as well as conceptual shortfalls (e.g., Herschel 1785; Kapteyn 1922). Over time, it was established that the Milky Way's scale height is inversely proportional to the masses of stars sampled (Gilmore & Reid 1983; Gilmore 1984; Siegel et al. 2002). Initially, many of the Galactic models were focused on relatively luminous giant stars and rarely addressed (sub)stellar objects due to completeness issues (see for reviews of star counts and Galactic structure; Bahcall 1986; Gilmore et al. 1989; King et al. 1990; Majewski 1993).

Interest has now shifted to the spatial distribution of (sub)stellar objects, in part because they are possibly the most significant interlopers in studies of extremely high redshift objects (see e.g., Caballero et al. 2008), but also because these are physically some of the longest lived objects. Consequently, any deep high-redshift survey, espe-

cially in the near-infrared, undertaken with the Hubble Space Telescope automatically becomes a census of the smallest Milky Way stars. More importantly, these objects constitute the most numerous and oldest population of stars in the Galactic disk. For instance, Pirzkal et al. (2005) determined the scale-height of different types of dwarfs from the Hubble Ultra Deep Field (HUDF, Beckwith et al. 2006). Ryan et al. (2005) found L and T dwarfs in a small set of ACS parallel observations. Stanway et al. (2008) and Pirzkal et al. (2009) determined the Galactic scale-height of M-dwarfs from the Great Observatories Origins Deep Survey fields (GOODS, Giavalisco et al. 2004). Ryan et al. (2011) added a search of early WFC3 pure-parallel fields for L and T dwarfs. These studies gradually improved statistics on L, T and M-dwarfs to several dozens of objects.

The identification of these Galactic dwarfs in images is difficult as one needs both high-quality data to distinguish from extragalactic sources and a good understanding of the initial mass function or the local density of these objects as a class. Two of the above studies (Pirzkal et al. 2005, 2009) benefited from spectroscopic identification of the dwarf subtype in the HST/ACS grism spectra of the HUDF and GOODS fields (the GRAPES<sup>6</sup> and PEARS<sup>7</sup> projects respectively). Combined with an in-

<sup>1</sup> Leiden Observatory, Leiden University, P.O. Box 9513, 2300 RA Leiden, The Netherlands. [benne.holwerda@rassd.esa.int](mailto:benne.holwerda@rassd.esa.int), [twitter: benneholwerda](https://twitter.com/benneholwerda)

<sup>2</sup> Research Fellow, European Space Agency, ESA-ESTEC, Keplerlaan 1, 2200 AG Noordwijk, the Netherlands

<sup>3</sup> University of Melbourne?

<sup>4</sup> Department of Natural Sciences College of Arts, Sciences and Letters, University of Michigan-Dearborn 4901 Evergreen Road, Dearborn, MI 48128, USA

<sup>5</sup> Space Telescope Science Institute, Baltimore, MD 21218, USA

<sup>6</sup> Grism ACS Program for Extragalactic Science, see Pirzkal et al. (2004)

<sup>7</sup> Probing Evolution And Reionization Spectroscopically, see Pirzkal et al. (2009).

dex of stellarity in the direct image, this made identification of the dwarfs near certain. Alternatively, Kilic et al. (2005) used high-precision proper motion to identify the Galactic objects. Once an object has been identified as a candidate dwarf, its luminosity distance must be estimated, which requires accurate (sub)typing. Without direct spectra, we will show that this can be readily achieved with sufficient color coverage from the optical to the near-infrared. A dwarf census including subtype and distance, can answer several outstanding issues regarding the shape of the Milky Way traced by its most numerous stellar members.

Pirzkal et al. (2009) found, like Stanway et al. (2008), an odd discrepancy in the numbers of M-dwarfs: there are 24% more M-dwarfs in the Northern than in the Southern GOODS field. Since our vantage point in the Milky Way is above the plane of the disk, one would expect the Southern GOODS fields to have more M-dwarfs. However, as present, this discrepancy has only been determined from two sight-lines out of the Galaxy, so it is still possible this may be source count field-to-field variance. By studying the older stellar population content of our Galaxy along many sight-lines down to the faintest possible magnitude, we can directly observe and measure the shape of the thin Galactic disk as traced by the old stellar population.

In order to improve our understanding of the contribution of faint dwarfs to Galactic structure, we will need much improved statistics to compare against Milky Way structure models. We use the recent *HST/WFC3* Pure Parallel searches for bright high-redshift galaxies to find Milky Way dwarfs and determine the parameters of their distribution in the Milky Way disk (Trenti et al. 2011; Yan et al. 2010; Bradley et al. 2012). Thus far, based on *HST* imaging, the disk scale height for dwarfs has been found to be: 300 pc (Table 1). (Zheng et al. 2001),  $400 \pm 100$  pc (Pirzkal et al. 2005),  $350 \pm 50$  pc, (L, T dwarfs Ryan et al. 2005),  $370 \pm 65$  pc (for M4–M9 dwarfs) and  $300 \pm 70$  pc (for M0–M9 dwarfs, Pirzkal et al. 2009) and  $300 \pm 25 (\pm 31 \text{ systematic})$  pc. ( $>M8$ , Ryan et al. 2011).

The goal of this paper is to explore the reality of the North-South difference in M-dwarf counts and to accurately determine the scale-height of our Milky Way as traced by M-dwarfs. Previously, Ryan et al. (2011) investigated the L and T dwarf content, here we focus our analysis on the M dwarfs.

The paper is organized as follows, §2 reports the properties of the *HST/WFC3* observations we use, §3 discusses how we generate the relevant SEXTRACTOR catalogs, §4 presents our observational calibration of morphological identification of stars, M-dwarfs specifically, and subsequent sub-typing of the M-dwarfs. §5 presents our catalog of dwarfs in the BoRG fields and briefly discusses the validity of our morphological selection. In §6 we discuss the North/South difference, the Galactic scale-height as a function of dwarf subtype. §7 lists our conclusions and outlines future work.

## 2. WFC3 OBSERVATIONS

We use three WFC3 data-sets for this project: the CANDELS public v0.5 data-release, and the Early Release Science mosaic, both in the GOODS-South field for calibration and characterization of known M-dwarfs, and the BoRG pure-parallel observations for the detection of

**Table 1**  
The scale-heights for the thin disk of dwarf stars from the literature.

Milky Way Scale Height ( $z_0$ ) (pc.)	Reference	type stars
300	Zheng et al. (2001)	
$400 \pm 100$	Pirzkal et al. (2005)	
$350 \pm 50$	Ryan et al. (2005)	L, T dwarfs
$370 \pm 65$	Pirzkal et al. (2009)	M4–M9 dwarfs
$300 \pm 70$	Pirzkal et al. (2009)	M0–M9 dwarfs
$300 \pm 25 \pm 31$	Ryan et al. (2011)	$>M8$

new Galactic M-dwarfs.

**Table 2**  
Summary of the WFC3 observations of BoRG, CANDELS (v0.5) and ERS on GOODS-S.

	BoRG	CANDELS	ERS
Filters	<i>F125W</i> , <i>F160W</i> , <i>F098M</i> , <i>F606W (F600L)</i>	<i>F125W</i> <i>F160W</i>	<i>F125W</i> <i>F160W</i> <i>F098M</i>
pixelscale	$0''.08$	$0''.06$ (resampled to $0''.08$ )	$0''.08$
PSF	$0''.12$	$0''.12$	$0''.12$
Exposure times (seconds)			
<i>F125W</i>	700-5100	1000	5017.61
<i>F160W</i>	500-3900	1050	5017.61

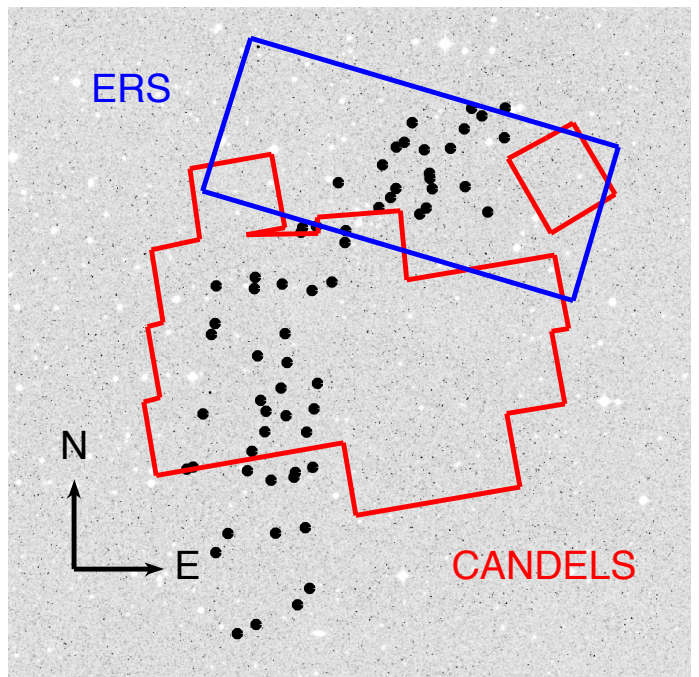


**Figure 1.** The GOODS South field with the The CANDELS v0.5 data-release of the deep part of the survey (red) and the Early Release Science mosaics (blue) overlaid on a digital sky survey image. The black circles mark the PEARS-identified stars.

### 2.1. CANDELS GOODS-S observations

The Cosmic Assembly Near-IR Deep Extragalactic Legacy Survey (CANDELS, Grogin et al. 2011; Koekoer et al. 2011) is designed to explore galaxy evolution, from redshift  $z = 1.5$  to  $\sim 8$ . The survey is designed to cover approximately  $800 \text{ arcmin}^2$  and is divided into two parts; CANDELS/Deep survey on both GOODS-N and GOODS-S and CANDELS/Wide covering GOODS as well as the EGS, COSMOS, and UDS fields. Data from the survey are non-proprietary and are published in a series of data-releases as soon as reduced to scientific quality (see <http://candels.ucolick.org>). In this paper we use the v0.5 data-release of the GOODS-South field, the first epoch of the CANDELS/Deep survey. Exposure times and sensitivity are very similar for this initial mosaic to the BoRG pure-parallel observations (Table 2) in the two near-infrared channels ( $F125W$  and  $F160W$ ). We resampled the CANDELS  $F125W$  and  $F160W$  mosaics to a pixel scale of  $0''.08$  using DRIZZLE (Fruchter & Hook 2002) to conform to the BoRG standard. For subsequent analysis, we only use a sub-section of this field (Figure 1), where PEARS and CANDELS coverage overlap.

### 2.2. Early Release Science WFC3 mosaic in Goods-South

The WFC3 imaging of the GOODS-S field is from the Early Science Release (ERS Windhorst et al. 2011) (see the footprint information at [http://candels.ucolick.org/survey/tile\\_maps/GOODS-S.html](http://candels.ucolick.org/survey/tile_maps/GOODS-S.html) and Figure 1). The 10 WFC3 fields in the ERS program were also imaged with the  $F125W$ ,  $F160W$  and  $F098M$  filters, the reason it was included in the Ryan et al. (2011) sample. We retrieve the data from the Hubble Legacy Archive ([www.hla.stsci.edu](http://www.hla.stsci.edu)), and combined these into a mosaic using SWARP (<http://www.astromatic.net/software/swarp>) to the same pixel scale as the BoRG fields. Figure 1 shows the overlap of this mosaic with the PEARS-S survey (Pirzkal et al. 2009).

### 2.3. BoRG

Our principal data-set is the WFC3 data from the BoRG (Brightest of Reionizing Galaxies, HST GO/PAR-11700, Trenti et al. 2011; Bradley et al. 2012) survey to identify Milky Way dwarf stars from their morphology and color. The BoRG observations are undithered HST/WFC3 conducted in pure-parallel with the telescope pointing to a primary spectroscopic target with the Cosmic Origin Spectrograph (typically a high- $z$  QSO at high Galactic latitude). The limitations for such observations are primarily that no dithering strategy can be used (final images are at WFC3 native pixel scale) and total exposure times are dictated by the primary program.

The program's initial aims were to obtain  $176 \text{ arcmin}^2$  of sky in 38 pointings, using four WFC3 filters ( $F606W$ ,  $F098M$ ,  $F125W$ , and  $F160W$ ). An extension of the BoRG program in Cycle-19 brought more parallel observations and the full reproduced set of 68 images is presented in Bradley et al. (2012). Because lines of sight are independent and well separated on the sky mostly at high Galactic latitudes ( $|b| > 20^\circ$ , see Figure 2), the BoRG survey samples the Milky Way disk away from the plane better than single sight-lines (e.g., the GOODS or H(U)DF

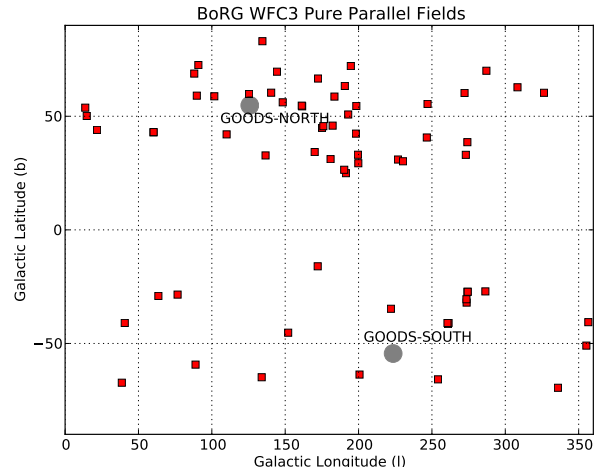


**Figure 2.** The position of the 68 unique WFC3 Pure Parallel Fields in Galactic coordinates (red squares). The sampling of the Milky Way disk structure of substellar objects is much better than the two lines-of-sight by the GOODS/PEARS fields (black circles). We discard one field (borg\_1815-3244) for its low latitudes and line-of-sight through the plane of the disk and close of the center of the bulge.

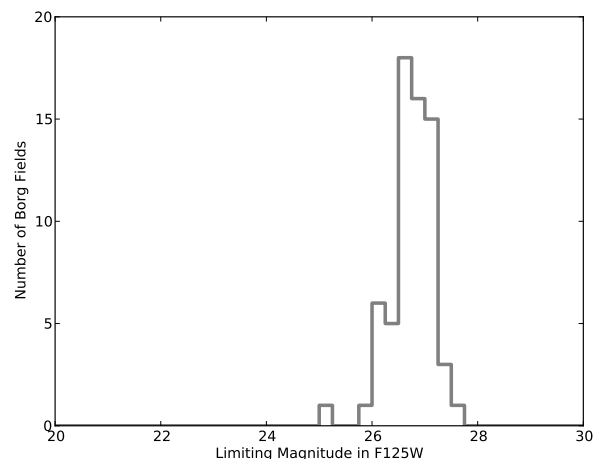


**Figure 3.** The distribution of limiting magnitude in the  $F125W$  filter from Bradley et al. (2012). Photometric detections are reliable down to 26 magnitude.

fields). The BoRG data-set used here is the second data-release of 68 WFC3 fields (Table 13) for a total of approximately  $209.9 \text{ arcmin}^2$  as described in detail by Trenti et al. (2011) and Bradley et al. (2012), including some reprocessed fields from another pure-parallel program with similar science goals (Hubble Infrared Pure Parallel Imaging Extragalactic Survey, HIPPIES, HST GO/PAR-11702, Yan et al. 2010). We use the WFC3 data-products generated by the BoRG team (see for details Bradley et al. 2012). This is a standard multi-drizzle reduction of these undithered WFC3 data with Laplacian edge detection (van Dokkum 2001) to the individual FLT files to mitigate detector hot pixels and cosmic rays. Stellar objects are not affected by this filtering.

The BoRG survey is designed to identify relatively

bright ( $m_{F125W} \leq 27$ ) high-redshift galaxies from their broad-band colors using the Lyman-Break technique (Steidel et al. 1996). The primary aim of the survey is to select redshift  $z \sim 7.5$  galaxies as *F098M* dropouts. Two near-infrared filters (*F125W* and *F160W*) are used for source detection and characterization down to 26 mag (Figure 3). One optical filter (*F606W* or *F600LP* in the case of the HIPPIES survey) is used to control contamination from lower redshift sources;  $z \sim 1.5$  compact galaxies, AGNs, and cool Milky Way stars. Our interest here now goes to the latter of these interlopers. Given the near-random pointing nature of the pure-parallel HST program (higher Galactic Latitude objects are preferred for COS targets), the BoRG fields are minimally affected by field-to-field (cosmic) variance (Trenti & Stiavelli 2008). Therefore, this catalog is uniquely positioned to set constraints on the number density of unresolved sources, either Milky Way stars or  $z \sim 8$  galaxies.

A recent BoRG observing campaign (BoRG13) is presented by Schmidt et al. (*in preparation*), which includes approximately 50 arcmin<sup>2</sup> of new data (13 fields) and deeper observations of two previous BoRG pointings. This brings the total J-band area of the BoRG survey to  $\sim 350$  arcmin<sup>2</sup> makes BoRG the largest existing near-infrared survey with HST, e.g., compare with CANDELS wide (260 arcmin<sup>2</sup>) or deep (120 arcmin<sup>2</sup>). We include nine BoRG13 fields as additional lines-of-sight in our sample (see Table 13).

### 3. CATALOG GENERATION

To construct the catalogs for the BoRG Fields, we ran SEXTRACTOR (Bertin & Arnouts 1996; Holwerda 2005) with similar settings as Trenti et al. (2011) but set to include `MU_MAX`,  $r_{50}$  and other morphological information. Source detection was done in the *F125W* image, with the other filters run in dual-image mode. The multi-drizzle weight files were used as RMS maps (once normalized, following the prescription in Casertano et al. 2000, `WEIGHT_TYPE=MAP_RMS`), but scales appropriately to reflect the noise correlation introduced. The photometric zero-points are from Dressel et al. (2010); Windhorst et al. (2011): *F606W*: 26.08, *F600LP*: 25.85, *F098W*: 25.68, *F125W*: 26.25, and *F160W*: 25.96 respectively with  $A_V$  corrections derived for each individual field (Table 13). These settings resulted in 93106 objects in the BoRG survey.

### 4. CANDELS AND ERS CALIBRATION CATALOGS

We generated SEXTRACTOR v2.8 catalogs with the same settings as above for the section of the resampled CANDELS mosaic, which includes the PEARS-S coverage (Figure 1) to obtain *F125W* and *F160W* luminosities and morphological information for the spectroscopically identified M-dwarfs. Optical magnitudes for these are from ACS photometry presented in Pirzkal et al. (2009). The overlap between the PEARS-S survey and CANDELS mosaic is a sample of 24 M-dwarfs (Table 5). We will use their morphology to select bona-fide stars in the *F125W* images and their colors to select and sub-type the M-dwarfs.

A second calibration catalog of 22 bona-fide PEARS-identified M-dwarfs is constructed based on the ERS mosaics (Table 6). The ERS mosaic pixel scale was set to be identical to the BoRG fields and all the SEXTRACTOR

parameters are kept identical to the BoRG ones. Similar to the CANDELS and BoRG catalog, detection was done in *F125W* with the catalogs in *F160W*, *F098M* and *F606W* or *F600LP* in dual mode for the respective photometry. Cross-correlation with the PEARS identified sources used the published right ascension and declination from Pirzkal et al. (2009) converted to pixels but due to some lingering issues with the wcs coordinates in the ERS data, we are less certain about the cross-identification than in the CANDELS data ( $\sim 0''.1$  uncertainty in position). Because of these issues and the uncertainty in the flux calibration between CANDELS and the ERS mosaics (Figure 4), we adopt the CANDELS mosaic as our primary calibrator for morphological selection and sub-typing and the ERS to calibrate the color-color selection and as a check of the CANDELS data.

#### 4.1. CANDELS and ERS photometry

We used the same zeropoints for all the filters as those used for the BoRG survey (Trenti et al. 2011; Bradley et al. 2012) and ERS (Windhorst et al. 2011). However, the ERS data was taken when the WFC3 instrument was still cooling down and hence one could expect slightly different WFC3 performance between the CANDELS and ERS photometry catalog. To check, we identified stars (using the  $r_{50}$  criterion below) in the full ERS mosaic and cross-correlated these with the full CANDELS catalog (derived from the  $0''.06$  mosaic). The overlap is 13 point-sources. Figure 4 shows the difference SEXTRACTOR magnitudes for these stars between the CANDELS and ERS mosaics in the *F125W* and *F160W* filters.

Discarding the faintest objects as their stellarity becomes uncertain (Figure 5), the mean difference between the overlap stars for different apertures ( $m_{F125W} < 24$ ,  $m_{F160W} < 23.5$ ) are listed in Table 3. We take the differences in the `MAG_APER` as the most reliable as these were computed for identical-size apertures. Because we used the `ASSOC` option in SEXTRACTOR, the placement of these apertures could conceivably be slightly different (typically less than a pixel difference) but this is not enough to explain the offset in photometry.

Thus, for the following, we correct the ERS photometry by subtracting 0.43 and 0.39 for the *F125W* and *F160W* respectively. However, we lack a similar information for the *F098M* filter and adopt a correction of 0.4 magnitude, the mean of the correction for the *F125W* and *F160W* correction.

**Table 3**

The difference and rms between the CANDELS and ERS magnitudes for the *F125W* and *F160W* filters. The aperture for `MAG_APER` is  $0''.48$  (8 and 6 pixels respectively).

Filter	MAG_ISO	MAG_AUTO	MAG_APER
F125W	-0.34 (0.23)	-0.40 (0.26)	-0.43 (0.19)
F160W	-0.26 (0.11)	-0.28 (0.10)	-0.39 (0.10)

#### 4.2. Morphological Identification of Stars

To identify the low-mass dwarfs in our catalogs, we opt for a strict morphological selection to allow the color

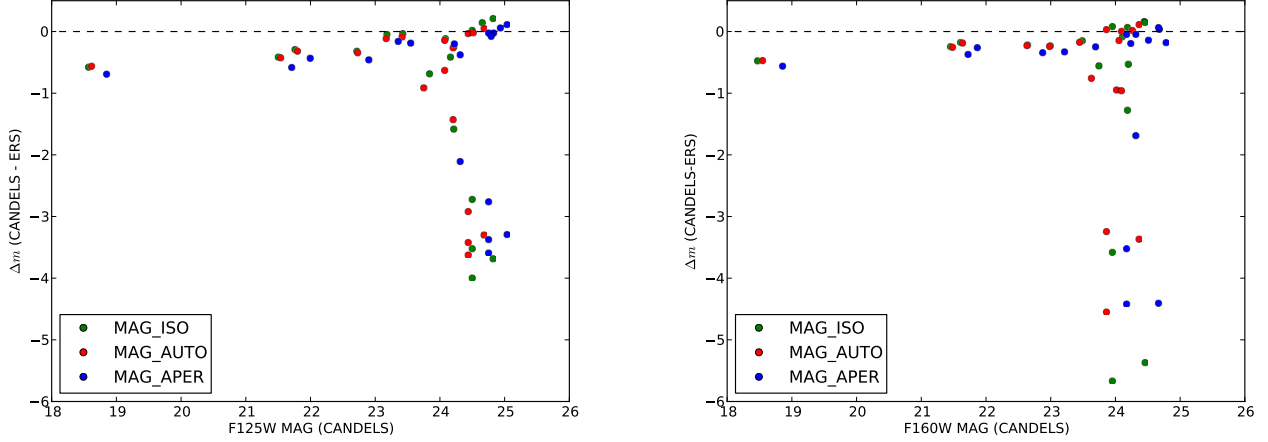


**Figure 4.** The difference in magnitude between the CANDELS and ERS mosaics. The CANDELS `SEXTRACTOR` catalog was generated from the  $0''.06$  pixel scale, full mosaic. Cross-correlation with the ERS mosaic yielded 13 stellar objects. There is an offset in both filters between the mosaics.

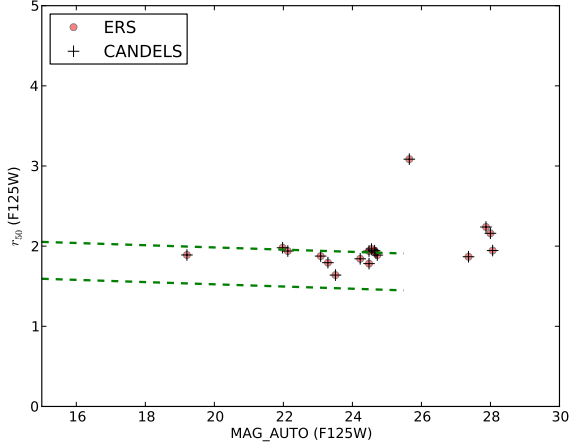


**Figure 5.** The relation between `MAG_AUTO` and half-light radius ( $r_{50}$ ) for the common objects between the CANDELS v0.5 field and the ERS (see Figure 1). The green lines are the stellarity criterion for the half-light radius. Beyond `MAG_AUTO`~24, the stellarity of these objects is doubtful.

information to be used for identification of the stellar type and subtype. There are several `SEXTRACTOR` parameters cuts in use to identify unresolved sources, all of them a variation on a concentration index; the `CLASS_STAR`, native to `SEXTRACTOR`, the half-light or effective radius ( $r_{50}$ ) used by Ryan et al. (2011), the flux ratio between to pre-defined apertures, e.g., the stellarity index  $S_2 = \text{MAG}_{\text{aper}(1\text{pix})} / \text{MAG}_{\text{ISO}}(\text{F125W})$  in Pirzkal et al. (2009), and the relation between the brightest pixel surface brightness and total source luminosity ( $\text{MU\_MAX} / \text{MAG\_AUTO}$ , Holwerda 2005; Holwerda et al. 2005; Leauthaud et al. 2007, who used it to discard stars.).

Using the M-dwarf catalog for CANDELS, we define three morphological criteria: one based on the stellarity index ( $S_2$ ), one on the  $\text{MU\_MAX} / \text{MAG\_AUTO}$  ratio, and one for the half-light radius ( $r_{50}$ ) for `F125W` catalog. If we fit the relation between  $S_2$ ,  $\text{MU\_MAX} / \text{MAG\_AUTO}$

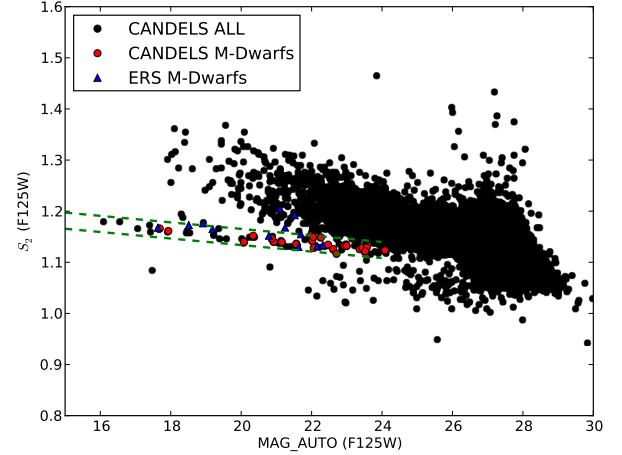


**Figure 6.** The  $S_2$  parameter for the CANDELS subfield of Figure 1, (crosses) and the bona-fide M-dwarfs identified in this field by PEARS (red points). The green dashed lines indicate our  $S_2$  selection criterion.

and  $r_{50}$  with `MAG_AUTO` for these M-dwarf we get:

$$|S_2 + 0.0065 \times \text{MAG\_AUTO} - 1.18| < 0.016 \quad (0.018), \quad (1)$$

the relation between  $\text{MU\_MAX}$  and the luminosity (`MAG_AUTO`),

$$\left| \frac{\text{MU\_MAX}}{\text{MAG\_AUTO}} - 0.0085 \times \text{MAG\_AUTO} - 0.65 \right| < 0.019 \quad (2)$$

and the half-light radius ( $r_{50}$ ),

$$|r_{50} - 0.014 \times \text{MAG\_AUTO} - 2.03| < 0.23. \quad (3)$$

with the variance in the relation determined from the scatter of the M-dwarfs around the fit. Thus, by definition these criteria will typically select all 24 M-dwarfs in the CANDELS field. Figure 6, 7, and 8 show these three criteria for objects in the CANDELS sub-field catalog with the PEARS M-dwarfs highlighted. For comparison,



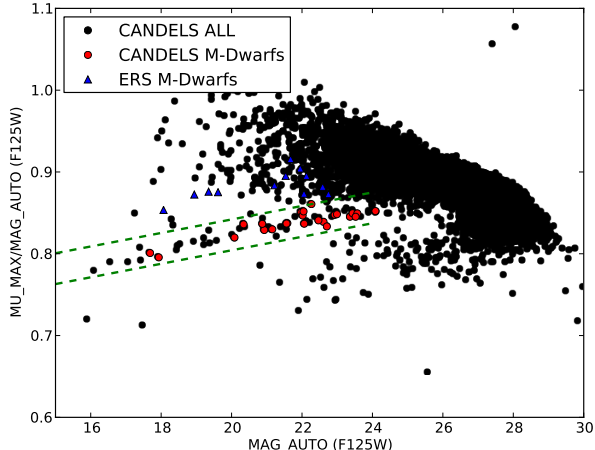


**Figure 7.** The  $\text{MU\_MAX/MAG\_AUTO}$  parameter for the CANDELS subfield of Figure 1, (crosses) and the bona-fide M-dwarfs identified in this field by PEARS (red circles). The green dashed lines indicate our  $\text{MU\_MAX/MAG\_AUTO}$  selection criterion.

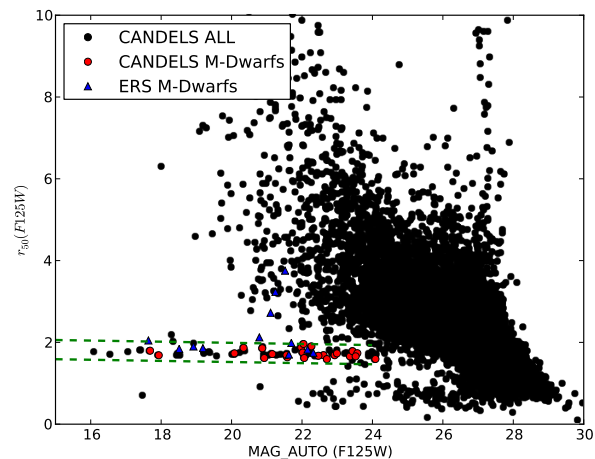


**Figure 8.** The  $r_{50}$  parameter (half-light radius) for the CANDELS subfield of Figure 1, (crosses) and the bona-fide M-dwarfs identified in this field by PEARS (circles). The green dashed lines indicate our  $r_{50}$  selection criterion.

the ERS M-dwarfs are also marked. Table 4 shows how many stars they select in the CANDELS field.

Our goal is to define criteria that would successfully select the PEARS stars. We note that our calibrators are the confirmed M-dwarfs and that some of those objects selected as stars in the CANDELS field are still Galactic stars, just not M-dwarfs. All three criteria work remarkably better than  $\text{CLASS\_STAR}$ , selecting stars with little contamination for objects brighter than  $m_{F125W} < 24$  (Figures 6–9). However, there is a marked difference in efficiency between the  $S_2$  and  $\text{MU\_MAX/MAG\_AUTO}$  criteria and the  $r_{50}$  criterion in the 24–25.5 mag range. The half-light radius criterion is much stricter than the other two (Table 4), i.e., it includes most of the PEARS identified M-dwarfs but includes much fewer objects from CANDELS than the other two criteria.

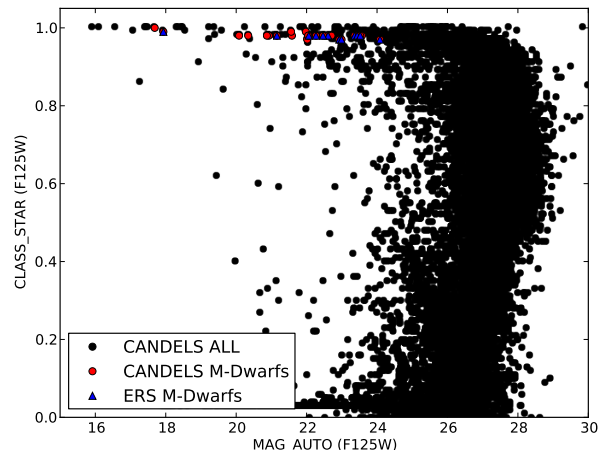


**Figure 9.** The  $\text{CLASS\_STAR}$  parameter from SEXTRACTOR for the CANDELS subfield of Figure 1, (crosses) and the bona-fide M-dwarfs identified in this field by PEARS (circles).

**Table 4**

The number of selected objects in the CANDELS/GOODS-S mosaic section (Figure 1) for the three different criteria separately and in combinations. The mosaic contains 24 bona-fide M-dwarfs and we note their selected number as well. Stricter limits resulted in some of those not being selected.

criteria	CANDELS < 25.5	PEARS M-dwarfs
$S_2$	216	24
$\text{MU\_MAX/MAG\_AUTO}$	331	23
$r_{50}$	120	23

The half-light parameter was used by Ryan et al. (2011) in some of these fields to select faint dwarf stars ( $1.2 \leq r_{50} \leq 1.8$  pixels with their pixelscale set to  $0''.09$ ). Our calibration here shows that this selection criterion is even a little lenient (the selection range can even be narrower), allowing for the different pixel scales, but works very well for the M-dwarfs in these fields.

#### 4.2.1. ERS catalog check

The 22 M-dwarfs in the ERS catalog are also plotted in Figures 6–9 to serve as a check for the morphological selection. Their positions in these figures reveal a sensitivity in both the  $S_2$  and the  $\text{MU\_MAX/MAG\_AUTO}$  relations for unresolved objects to the pixel scale. The  $r_{50}$  criterion is less sensitive to the scale of the pixels. Most likely, this is because it is computed from the growth curve of an objects, i.e., the ordered list of pixels. The other two criteria both depend on an aperture of a single pixel and hence are more sensitive to the pixelscale. Several of the identified objects in the ERS catalog are well away ( $r_{50} > 2$  pixels) from those values expected for stars, i.e., unresolved objects. These are likely either mis-identifications in the ERS field or blends with other objects or artifacts.

The comparison shows that both the  $r_{50}$  and the  $\text{MU\_MAX/MAG\_AUTO}$  work well for stellar selection brighter than 24 mag and the  $r_{50}$  includes much less in-

terlopers down to 25.5 mag. The practical limit of 24 mag for PEARS identified M-dwarfs in  $F124W$  would limit identifications to distances from 3.2 to 36.3 kpc depending on M-dwarf subtype (M9-M0 respectively), or some 10-100 thin disk scale-heights. We treat our sample as uncontaminated, photometrically accurate, and calibrated with the CANDELS M-dwarfs up to this conservative limit, which is still two magnitudes above the BoRG photometric detection limit (Figure 3).

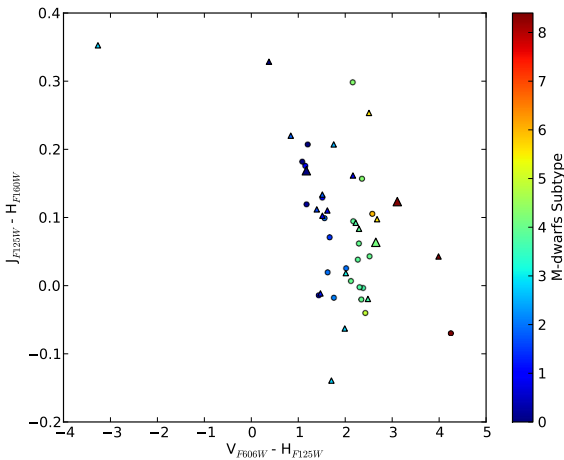


**Figure 10.** The relation between the  $F606W-F125W$  and  $F125W-F160W$  colors for the M-dwarf sub-type (0-8) determined from the GOODS, CANDELS and ERS data for the PEARS spectroscopically identified M-dwarfs.

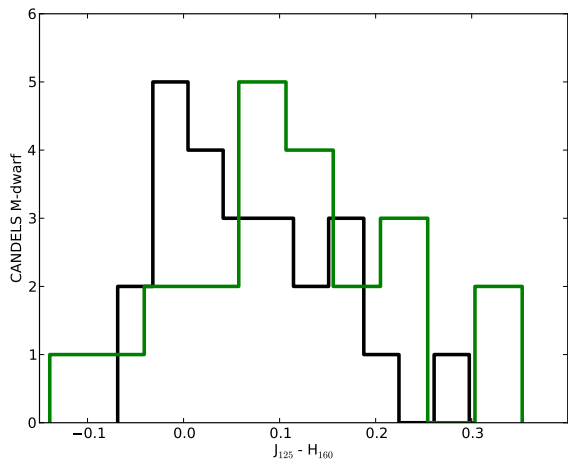


**Figure 11.** The histogram of the  $F125W-F160W$  colors from CANDELS and ERS of the PEARS spectroscopically identified M-dwarfs.

#### 4.3. M-Dwarf NIR color-color selection

The second part of the calibration is an empirical color-color selection for the M-dwarfs in the GOODS-S field. We base the M-dwarf selection in near-infrared colors

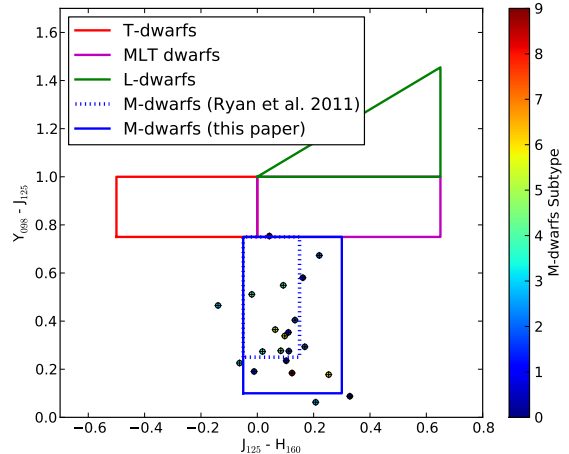


**Figure 12.** A plot of the  $F125W-F160W$  and  $F098M-F125W$  colors from the ERS of the 22 PEARS spectroscopically identified M-dwarfs.

because of the wide range in optical-near-infrared colors M-dwarf subtypes can display (Figure 10). To identify M-dwarfs, we require their  $J_{F125W} - H_{F160W}$  and  $Y_{F098M} - J_{F125W}$  color to be similar to the distribution of the PEARS-identified M-dwarfs. To find the J-H color range, we can use both the CANDELS as the ERS catalog but for the Y-J color, we must rely on the ERS catalog alone.

Figure 11 shows the distribution of  $J_{F125W} - H_{F160W}$  color for the PEARS M-dwarfs in the CANDELS and ERS fields. These are not in the range one would infer from Ryan et al. (2011), in their Figures 3 and 4 but wider by a few tenths of magnitudes. The ERS and CANDELS J-H colors are still different by  $\sim 0.1$  magnitude (Figure 11). We suspect that the PEARS M-dwarf  $F125W-F160W$  color distribution in CANDELS in Figure 11 is different than the distribution in Ryan et al. (2011) because their colors were derived from spectra convolved with appropriate filter response functions. There is however an under-reported drop in WFC3 detector sensitivity on the red side of the  $F160W$  filter (Andersen et al. *in preparation, private communication*). The  $F098M$  and  $F125W$  filters however, do not suffer from the detector sensitivity degradation at the red side. This could in part account for the small difference in J-H color of the CANDELS M-dwarfs, whose photometry we trust, with the position of M-dwarfs in Figure 3 in Ryan et al. (2011) or the difference in  $F125W-F160W$  color with the ERS as the detector was still cooling down (Figure 11)

The ERS mosaics is in the same NIR filters as the BoRG fields ( $F125W$ ,  $F160W$  and  $F098M$ ) and Figure 12 shows the position of the 22 objects matched to PEARS M-dwarfs in a J-H, Y-J color-color plot. We show the same color criteria as Figures 3 and 4 in Ryan et al. (2011). The width and position of the Y-J color criterion is close to what one would infer from Figure 3 in Ryan et al. (2011).

Based on both Figure 11 and 12, we define a near-infrared color-color criterion to select M-dwarfs in the BoRG survey;  $-0.05 < J - H < 0.3$  and  $0.1 < G - J < 0.75$  (the solid blue boxes in Figure 12 and 19 in addition

**Table 5**

The M-dwarfs identified by PEARS in the CANDELS field. The optical magnitudes are from Pirzkal et al. (2009) and the  $F125W$  and  $F160W$  magnitudes from our SEXTRACTOR catalog of the CANDELS field.

ID	Type	ra	dec	$m_{F435W}$	$m_{F606W}$	$m_{F775W}$	$m_{F850W}$	$m_{F125W}$	$m_{F160W}$
48173	4.0	53.220073	-27.854046	25.22	24.96	23.73	23.15	22.61	22.63
53237	4.0	53.194890	-27.848121	25.19	25.45	24.14	23.49	22.93	22.88
58796	1.5	53.173782	-27.841699	25.70	25.04	24.17	23.85	23.36	23.29
58826	4.3	53.189870	-27.841487	24.76	24.34	23.04	22.39	21.98	21.82
63079	1.0	53.181657	-27.836074	25.49	24.44	23.76	23.47	22.99	23.00
63028	3.7	53.213644	-27.835281	24.29	23.97	22.78	22.15	21.58	21.59
63752	3.9	53.189345	-27.834509	23.80	23.43	22.37	21.74	21.16	21.12
63993	2.0	53.170843	-27.833788	23.81	23.13	22.27	21.91	21.56	21.46
66572	8.4	53.191395	-27.830774	24.60	26.71	24.80	23.58	22.47	22.53
69522	6.0	53.183514	-27.826627	24.89	24.60	23.41	22.64	22.02	21.91
70032	3.9	53.169502	-27.825087	22.88	22.52	21.40	20.77	20.34	20.25
74670	1.0	53.181116	-27.817942	25.79	24.96	24.20	23.97	23.44	23.31
74928	4.0	53.192508	-27.815594	20.55	20.06	19.10	18.51	17.93	17.92
79699	4.0	53.210190	-27.808231	22.75	22.38	21.29	20.66	20.08	20.02
80618	2.0	53.181804	-27.808089	26.31	25.72	24.88	24.48	24.08	24.06
82885	0.2	53.208736	-27.804499	25.77	24.76	24.13	23.83	23.57	23.45
91263	0.9	53.171308	-27.793465	24.35	23.43	22.76	22.49	22.27	22.09
92395	2.1	53.193512	-27.792703	24.44	23.83	22.93	22.54	22.06	22.08
93532	2.0	53.208197	-27.791671	26.19	25.55	24.52	24.07	23.52	23.50
93841	4.9	53.182786	-27.791200	25.10	25.14	23.97	23.34	22.71	22.74
94206	4.3	53.163637	-27.790605	24.71	24.21	23.00	22.37	22.04	21.75
95752	3.8	53.193173	-27.788834	23.42	23.24	22.12	21.53	20.93	20.93
104030	0.0	53.158515	-27.777252	22.95	21.97	21.34	21.16	20.87	20.69
104673	0.0	53.158184	-27.773143	19.76	18.90	18.48	18.04	17.69	17.48

**Table 6**

The M-dwarfs identified by PEARS in the ERS mosaic. The optical magnitudes are from Pirzkal et al. (2009) and the  $F125W$  and  $F160W$  magnitudes from our SEXTRACTOR catalog of the ERS mosaic.

ID	Type	ra	dec	$m_{F435W}$	$m_{F606W}$	$m_{F775W}$	$m_{F850W}$	$m_{F125W}$	$m_{F160W}$
108497	1.7	53.093027	-27.735838	21.39	20.58	19.78	19.42	19.19	19.07
108014	2.0	53.057966	-27.735053	19.76	18.81	18.37	17.80	17.64	17.47
110839	2.0	53.089621	-27.733082	23.02	22.36	21.48	21.06	21.52	21.30
111269	3.0	53.113985	-27.732740	24.68	23.98	23.05	22.58	21.99	22.05
111982	6.0	53.107958	-27.728253	21.63	21.19	19.94	19.11	18.51	18.41
114688	0.0	53.086462	-27.724381	24.06	23.11	22.49	22.22	22.73	22.41
115223	4.0	53.105121	-27.724124	25.11	24.64	23.51	22.90	22.16	22.18
114563	6.0	53.069511	-27.723391	22.27	21.88	20.69	19.90	19.37	19.12
116612	4.0	53.134575	-27.721317	24.55	23.85	22.70	22.24	21.63	21.53
117391	1.3	53.087638	-27.719656	23.01	22.13	21.42	21.04	20.66	20.67
119050	2.7	53.087816	-27.717329	26.03	24.77	23.84	23.42	23.02	22.81
120814	4.2	53.111938	-27.713369	24.19	23.99	22.87	22.19	21.70	21.61
123686	5.3	53.090399	-27.706629	23.60	23.44	22.25	21.52	20.79	20.72
124539	8.7	53.076943	-27.706018	25.28	25.75	24.27	23.22	22.64	22.52
124624	1.0	53.104778	-27.705292	23.78	23.41	22.76	22.42	21.25	21.08
125478	9.0	53.100622	-27.703149	24.03	24.37	22.53	21.29	20.38	20.34
126754	1.0	53.049225	-27.701327	24.91	23.94	23.19	22.88	22.32	22.21
128173	3.3	53.069739	-27.697205	23.69	23.12	22.11	21.57	21.11	21.09
128247	2.0	53.096541	-27.694200	21.16	20.43	19.62	19.24	18.92	18.78
130804	1.0	53.060606	-27.691367	24.23	23.33	22.66	22.35	21.82	21.71
132690	3.0	53.066145	-27.687565	24.21	23.86	22.91	22.44	21.73	21.67
132690	3.0	53.065896	-27.687864	24.21	23.86	22.91	22.44	22.15	22.29



to the L, T and MLT boxes from Ryan et al. (2011).

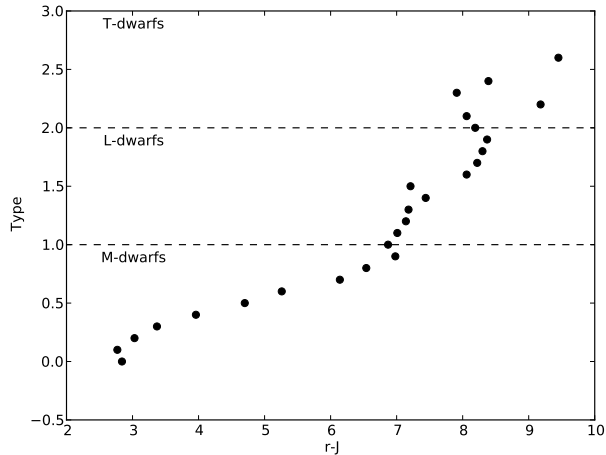


**Figure 13.** The relation between  $sdss-r-J$  color and spectral type from Hawley et al. (2002). M-dwarfs are 0-1 with subtype as the decimal, L-dwarfs are 1-2 with the subtypes as the decimal and T dwarfs are type 3 with the decimal the assigned subtype as molecular lines start to dominate the spectrum. The later type dwarfs do not show a good linear relation between a wide optical-near-infrared color and sub-type. However, they do show a redder color than all the M-dwarf subtypes and hence we can exclude all most stellar objects based on color.

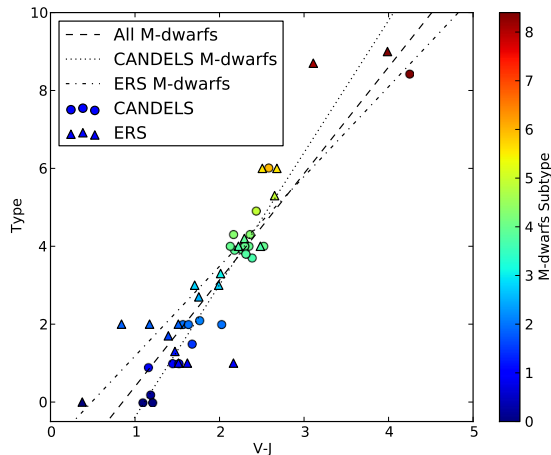


**Figure 14.** The relation between M-dwarf sub-type (0-8) and the  $F606W-F125W$  color relation as determined from the GOODS, CANDELS and ERS data for the PEARS spectroscopically identified M-dwarfs. There is a linear relation between this color and the subtype which we use to type the dwarfs in the BoRG WFC3 parallel fields. We show three fits; one based on all M-dwarfs ( $t < 6$ ), only the CANDELS M-dwarfs ( $t < 6$ ) and only the ERS M-dwarfs. We adopt the CANDELS relation as this sample is the cleanest with accurate photometry and similar exposure times as the BoRG fields.

#### 4.4. Sub-typing M-dwarfs

Our last calibration involving the PEARS identified M-dwarfs in the CANDELS and ERS mosaics of the

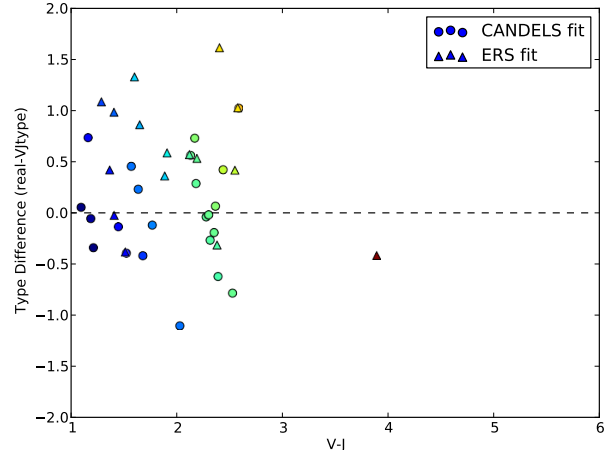


**Figure 15.** The residual between V-J inferred subtype and the spectroscopic subtype from PEARS for the M-dwarfs in the ERS and CANDELS data. The ERS  $F125W$  photometry may be shifted slightly still with respect to the CANDELS's (Figure 11) and this may account for the higher scatter for this subset.

GOODS-S field is to derive a color-subtype relation. Figure 13 shows the relation between  $r-J$  color and dwarf type from Hawley et al. (2002). M-dwarfs show a linear relation with a color, provided the baseline is long enough, i.e. optical to infrared. The later L and T dwarfs do not have such a clear relation.

Figure 14 shows the relation between the  $V_{F606W} - J_{F125W}$  color and the spectroscopic sub-type as determined by Pirzkal et al. (2009) for the 24 PEARS M-dwarfs in CANDELS and the 22 PEARS M-dwarfs in the ERS. They obtain a type from template fits to each ACS grism spectrum obtained for these objects. Because of design of the PEARS observations, there are oftentimes several spectra taken at different roll-angles. Cross-comparison between the spectral fits show that the uncertainty in the PEARS type classification is less than an M-dwarf subtype. We therefore take these spectral types as our gold standard for the classification of the stellar objects in the WFC3 parallel fields.

Figure 14 shows the relation between the V-J color and spectroscopic type from PEARS. We fit a linear relation to the CANDELS sample because it is the cleanest selection and photometry. The linear relation in the PEARS-identified CANDELS M-dwarfs can be expressed as:

$$M_{type} = 3.39 \times [V_{F606W} - J_{F125W}] - 3.78 \quad (4)$$

The M-dwarfs identified by PEARS in the ERS mosaic display more scatter than the CANDELS M-dwarfs but after correction of the  $F125W$  magnitudes (see above), the V-J colors and their PEARS subtype generally agree well with the relation derived from the CANDELS M-dwarfs, although some difference may remain (Figure 11).

Figure 15 shows the residual between the V-J color type and PEARS spectroscopic type. The PEARS M-dwarfs cover mostly subtype 0-5 and only a few M ( $t > 6$ ) are in this sample. Consequently, the color-subtype relation is most reliably for the earlier subtypes. Based in Figure 15, we take that our subtype based on V-J color

is accurate within a subtype. We adopt this relation to type M-dwarfs in the BoRG fields and compute type uncertainties as a result of the photometric uncertainty in the  $F606W$  and  $F125W$  magnitudes. We use the absolute magnitudes from Hawley et al. (2002) to compute distance moduli (Table 7) and infer distances.

**Table 7**

Absolute 2MASS J-band ( $F125W$ ) magnitudes of M-dwarfs from Hawley et al. (2002).

Subtype	$M_J$
0	6.45
1	6.72
2	6.98
3	7.24
4	8.34
5	9.44
6	10.18
7	10.92
8	11.14
9	11.43
10	11.43

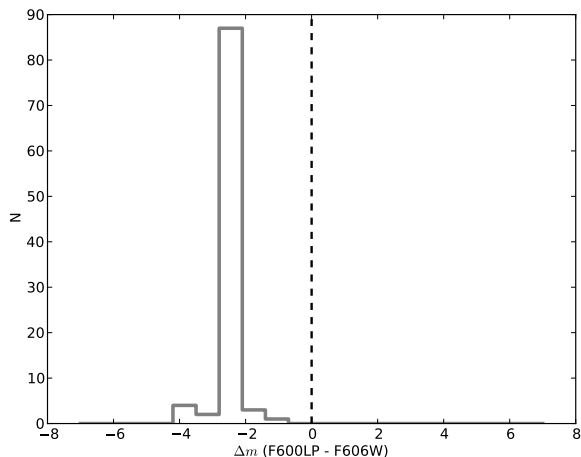


**Figure 16.** A histogram of the difference in  $F600W$  and  $F600LP$  MAGAUTO values for those stars in the M-dwarf near-infrared criteria for the three fields in the BoRG survey that have data in both filters.

#### 4.5. Substituting $F600LP$ for $F606W$ photometry

In the case of 24 fields in the BoRG survey,  $F606W$  photometry is not available. These fields come from the HIPPIES or COS-GTO parallel observations which opted for  $F600LP$  rather than  $F606W$ . The  $F600LP$  filter has a slightly different width compared to the  $F606W$  and a different central wavelength (closer to Johnson-I). Fortunately, there are three fields for which both  $F606W$  and  $F600LP$  data is available. We compared the  $F606W$ - $F600LP$  colors for those objects already pre-selected by their near-infrared color and morphology as likely M-dwarf to assess the impact of the change of filters. Figure 16 shows the histogram of the color difference between

the two bandpasses for M-dwarfs. The difference is substantial:  $F600LP - F606W = -2.65$  mag with a spread of 0.88 mag. Therefore we correct our  $F600LP$  photometry with this difference and increase the uncertainty in the photometry accordingly as well (which should be reflected in the subsequent automated typing).

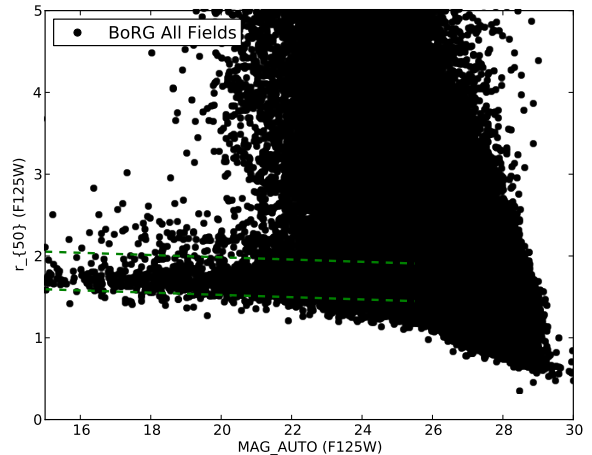


**Figure 17.** The  $F125W$  half-light radius as a function of magnitude for all the BoRG fields. The green dashed lines are the selection criterion from equation 3 to identify stars in these fields. Objects below the bottom green line are more likely to be defects (e.g. remaining hot pixels etc.).

## 5. STARS IN THE BOR G WFC3 PURE-PARALLEL FIELDS

With the morphological and near-infrared color-color selection in hand, we now search the BoRG fields for M-dwarfs as well as other substellar types. Figure 17 shows the same parameter space as Figure 8 but with all the BoRG objects. Based on the  $r_{50}$  selection criterion, we find 1308 stars to 24 mag in  $F125W$  in the 59 WFC3 parallel fields. For comparison, Figure 18 shows the other morphology criteria. The  $r_{50}$  selection criterion seems the most appropriate for the BoRG fields as the locus of stellar points is within the criterion lines.  $S_2$  appears equally applicable but the  $MU\_MAX/MAG\_AUTO$  criterion shows a discrepancy compared to Figure 7. We suspect this is because the CANDELS data was originally at a different pixel size and this criterion is sensitive to the exact pixel scale of the image. Figure 17 validates therefore our adoption of the  $r_{50}$  criterion for the morphological selection of stars.

To identify the various subtypes of stars, we construct a NIR color-color diagram similar to Figure 3 in Ryan et al. (2011), as discussed above. Figure 19 shows this plot with the limits for our selection criteria for approximate types. In the BoRG SEXTRACTOR catalog, we identify 30 L-dwarfs, 1 T-dwarfs, 274 M-dwarfs and 29 M, L or T-dwarfs based on the color cuts. The M-dwarf sample is the one of interest here. Tables 14, 15 and 16 list the properties of the identified stars which conform to the M, T and L-dwarf color cuts (Figure 19).

Subsequently, we sub-type the M-dwarfs according to equation 4. Figure 20 shows the histogram of M-dwarf subtypes in the BoRG fields as well as those objects in the

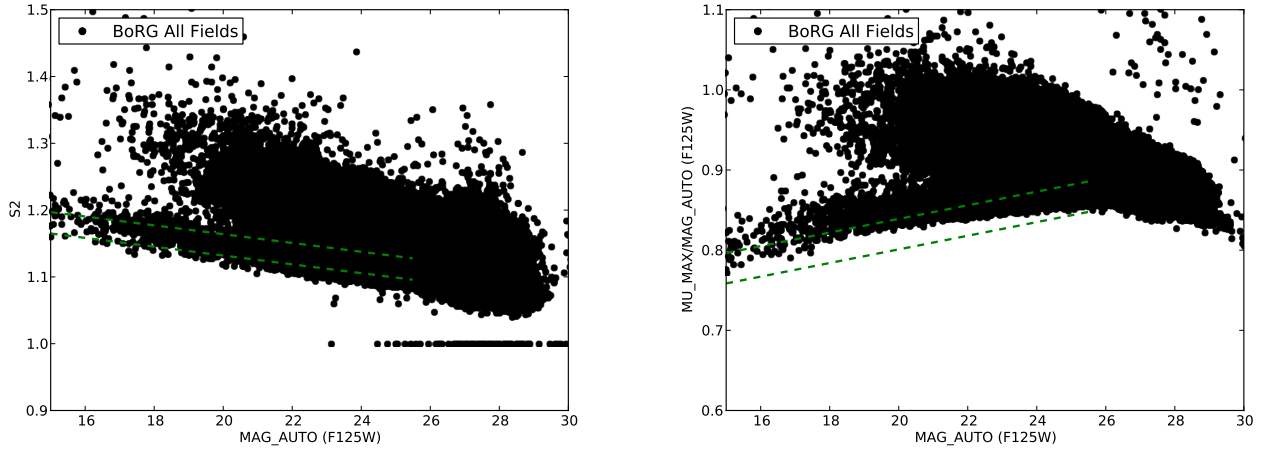


**Figure 18.** The two alternative morphological selections for star, for the BoRG data: the  $S_2$  and the  $\mu\_max/mag\_auto$  ratio.

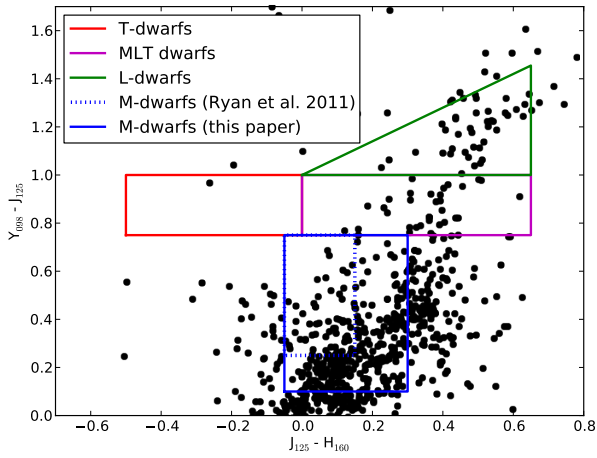


**Figure 19.**  $J_{F125W} - H_{F160W}$  versus  $G_{F098M} - J_{F125W}$  color diagram, similar to Figure 4 from Ryan et al. (2011), to distinguish between L, T, and M-dwarfs.

MLT box in Figure 19 for comparison. In effect this is an additional optical-near-infrared color criterion for M-dwarf selection as we will discard any star that could not be sub-typed. The dominant type in our M-dwarf sample is M0, specifically -1 to 1 type, not unexpectedly as these are the brightest and most numerous type of M-dwarf. There are almost as many later-type M-dwarfs (M4 and above) in the MLT color selection as in our exclusively M-dwarf box. However, as we note above, the later type classification is the most uncertain and in the MLT box, susceptible to L and T dwarf contamination.

There is still the possibility of contamination by Giants, sub-dwarfs and AGNs but we are confident that the morphological selection, luminosity limit and the color-color restriction select a very clean sample of Milky Way M-dwarfs.

### 5.1. Contamination by M-giants or M-type Sub-dwarfs

Bochanski et al. (2013) present a catalog of 404 M-giants from the UKIDSS survey DR8 ( $2400 \text{ deg}^2$ ,  $K < 17$ ), with these M-giants among the most distant stars

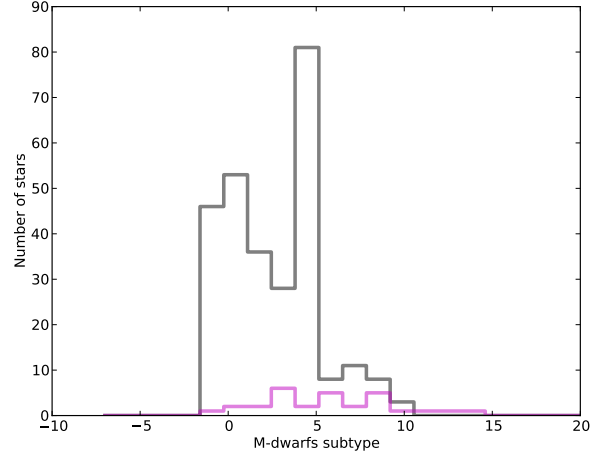


**Figure 20.** The histogram of M-dwarf types in our BoRG, inferred from equation 4. M0 and M1 are the most prevalent in the sample. As can be seen in the histogram, some of the stellar objects are not M-dwarfs but either other sub-stellar objects or possibly very distant (intergalactic?) M-giants.

belonging to the Milky Way. In principle, M-giants could be selected by our color selection. However, their on-sky density ( $4.3 \times 10^{-5}$  M-giants/arcmin<sup>2</sup>) makes it unlikely –not impossible– that even a single one is included in our selection. One could make a similar plausibility argument against very nearby M-type subdwarfs: the volume probed at close distances is comparatively small for a pencil beam survey.

## 6. DISCUSSION

Based on our bona-fide, morphologically and color selected M-dwarfs and the subsequent color sub-typing, we explore the North/South discrepancy, the Galactic thin disk scale-height as a function of subtype and whether or not we detect any additional Galactic component (Halo or Thick disk).

### 6.1. The North-South Divide

Pirzkal et al. (2009) found a North-South discrepancy between the number of M-dwarfs in the PEARs fields. They find 51 and 63 M0-9 dwarfs in the GOODS North and South fields respectively. Accounting for the different field sizes (41.61 arcmin<sup>2</sup> and 59.50 arcmin<sup>2</sup> respectively) this is equivalent to 1.23 and 1.06 M-dwarfs/arcmin<sup>2</sup>, an excess of 11% in the Northern field. Both GOODS fields are at similar Galactic Latitude and Pirzkal et al. note that because the Sun is North of the Galactic plane, the Northern excess appears to be a contradiction. Widrow et al. (2012) and Yanny & Gardner (2013) find similar North-South discrepancies in the SDSS catalog of (dwarf) stars in the solar neighborhood.

One of our science goals with this study was to establish if this a real discrepancy of due to natural field variance. The BoRG fields are over many more lines of sight and dividing these in Galactic Northern and Southern Fields: 134.5 and 72.1 square arcminute respectively. We count the M-dwarfs in those fields above 20° Galactic Longitude to avoid two Southern fields that sample more along the Galactic Plane.

We find on average  $1.157 \pm 0.088$  M-dwarfs of all types (M0-9) per arcmin<sup>2</sup> in the Northern fields and  $1.293 \pm 0.127$  per arcmin<sup>2</sup> in the Southern Galactic fields (Table 8), which agrees with the previously observed discrepancy. The Northern over density is the most pronounced in the early (M0-4) type M-dwarfs. Taking into consideration that for these early-types the statistics are more secure, and early-types dominate the grism sample of Pirzkal et al. (2009) (or the SDSS catalog), our counts corroborate the previously found North-South discrepancy. The Northern overdensity is most pronounced in the earliest types, gradually diminishing and reversing for late-type M-dwarfs (Table 8).

**Table 8**

Average number of M-dwarfs per square arcminute in Southern and Northern Galactic fields ( $|l| > 20^\circ$ ). M-dwarf numbers refer to those objects in the blue box in Figure 19. The last two columns are the ratio of M-dwarfs in Northern and Southern fields and the signal-to-noise of the noise.

	M-dwarfs		North / South	S/N
	North	South		
M-dwarfs	$1.157 \pm 0.088$	$1.293 \pm 0.127$	0.89	8.02
M0-4	$0.859 \pm 0.076$	$0.779 \pm 0.099$	1.10	6.45
M5-10	$0.210 \pm 0.038$	$0.465 \pm 0.076$	0.45	4.11
M0	$0.304 \pm 0.045$	$0.176 \pm 0.047$	1.73	3.27
M1	$0.156 \pm 0.032$	$0.151 \pm 0.043$	1.03	2.81
M2	$0.115 \pm 0.028$	$0.088 \pm 0.033$	1.31	2.23
M3	$0.088 \pm 0.024$	$0.075 \pm 0.031$	1.17	2.03
M4	$0.196 \pm 0.036$	$0.289 \pm 0.060$	0.68	3.58
M5	$0.095 \pm 0.025$	$0.364 \pm 0.068$	0.26	3.07
M6	$0.007 \pm 0.007$	$0.025 \pm 0.018$	0.27	0.82
M7	$0.041 \pm 0.017$	$0.025 \pm 0.018$	1.62	1.22
M8	$0.041 \pm 0.017$	$0.013 \pm 0.013$	3.23	0.93
M9	$0.020 \pm 0.012$	$0.038 \pm 0.022$	0.54	1.22
M10	$0.007 \pm 0.007$	$0.000 \pm 0.000$	0.00	0.00

## 6.2. A Local Over-density of M-dwarfs

A single field, borg\_1230+0750 stands out from the other BoRG fields with a local density of 21.4 M-

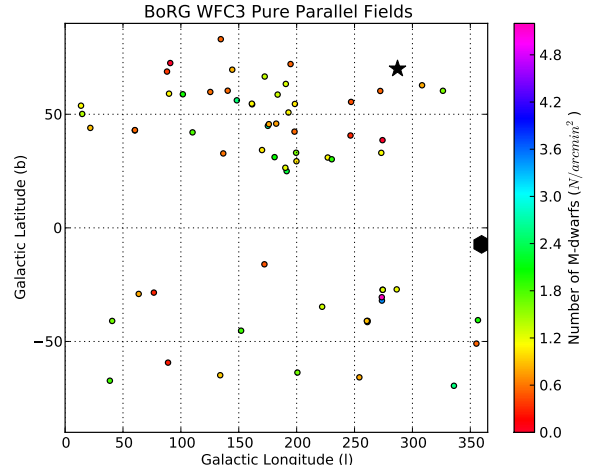


**Figure 21.** The distribution of BoRG fields with the number of M-dwarfs indicated. One field, borg\_1230+0750 (star) stands out with 22 M-dwarfs ( $\sim 20$  stars/arcmin<sup>2</sup>). We discard borg\_1815-3244 (black circle) for its low latitudes and line-of-sight through the plane of the disk and close of the center of the bulge.

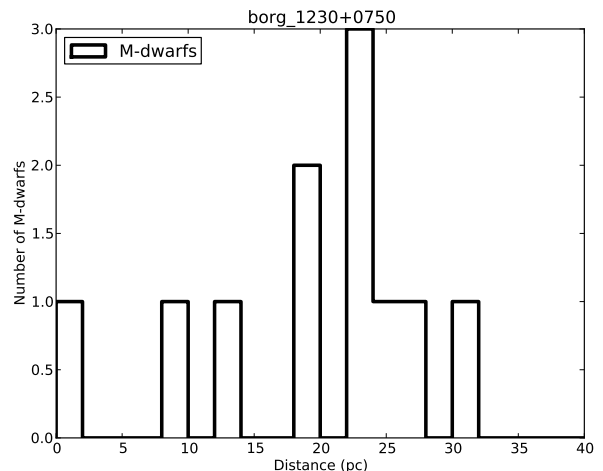


**Figure 22.** The distribution of M-dwarf distances in borg\_1230+0750, with a concentration at 20-25 kpc.

dwarfs/arcmin<sup>2</sup>. Such over-densities of faint Galactic stars are a possible contaminant for identifications of over-densities of high-redshift clusters (e.g., Trenti et al. 2012).

The Galactic position of this over-density ( $l = 287.119670593^\circ, b = 70.0322203957^\circ$ ) argues against a spiral arm or disk substructure to be the origin of this over-density. However, its position is exactly on the Sagittarius stellar stream (Majewski et al. 2003; Belokurov et al. 2006). Figure 22 shows the histogram of photometric inferred distances for the M-dwarfs in borg\_1230+0750. The distance of the over-density of M-dwarfs at 20-25 kpc. is also in line with these M-dwarfs belonging to the Sagittarius stream (Newberg et al. 2002; Belokurov et al. 2013) at this Galactic longitude.

The relative ease with which this stellar stream was identified in the BoRG data, shows that the future EU-

CLID mission will identify virtually *all* streams in the Milky Way halo from the dwarf stars alone.

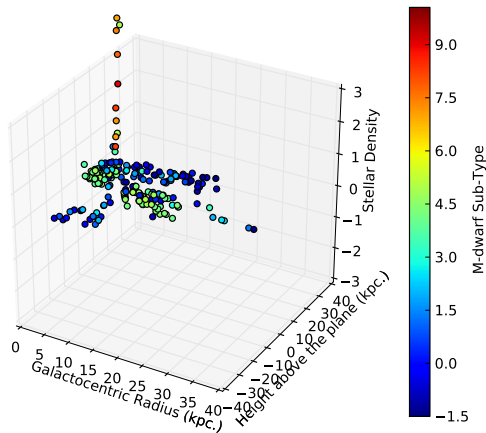


**Figure 23.** The computed volume for each M-dwarf as a function of Galactocentric radius, height above the plane. M-dwarf types as inferred from their optical-nir color.

**Table 9**

Local dwarf density from Figure 8 in Reid et al. (2008) and Cruz et al. (2007).

Subtype	Number within 20 pc.	
	Reid et al. 2008	Cruz et al. 2007
0	35	
1	50	
2	140	
3	90	
4	350	
5	400	
6	190	
7	170	21
8	45	21
9	60	11
10	42	3

### 6.3. Thin Disk Scale Height.

Previous studies based on small numbers of fields have already given us several estimates of the scale-height of the thin disk of the Milky Way in substellar objects (Table 1). The consensus appears to be a scale-height between 300 and 400 pc for the thin disk. For M-dwarfs, Jurić et al. (2008) find a thin disk of  $z_0 = 300$  pc. and a thick disk with  $z_0 = 900$  pc. from SDSS data.

To estimate the distances to each M-dwarf, we compute the distance modulus from the inferred sub-type (and hence absolute magnitude) and the apparent magnitude in F125W. We compute the Galactic radius and height above the plane for all M-dwarfs, based on their Galactic longitude, latitude and the above distance, assuming the position of the Sun is 27 pc. above the plane, and at a Galactocentric radius of 8.5 kpc from the Galactic center.

To compute the density at each M-dwarf’s position, we compute the physical area at the inferred distance of the BoRG survey field in which the dwarf was found and a binwidth of 1pc.

We discard one field (borg\_1815-3244) for two reasons: it is at low Galactic Latitude with a line-of-sight straight through the Galactic bulge (Figure 21), and secondly, there is only F600LP information available which makes subtyping of M-dwarfs more uncertain. This field contains 67 M-dwarf candidates but these are not used for the following analysis.

Figure 23 shows the distribution of radius and height above the disk for the 274 stars in the BoRG survey with their corresponding number density and type. The fainter late-sub-type M-dwarfs are in a localized thin disk and the bright early-sub-type (e.g., M0) correspond closer to the thick disk component.

We assume that the Galactic disk has the following parametric shape:

$$\rho(R, z) = \rho_0 \exp(-R/h) \operatorname{sech}^2\left(\frac{z}{z_0}\right), \quad (5)$$

where  $\rho(R, z)$  is the dwarf number density in a point in the disk,  $\rho_0$  is the central number density,  $R$  is galactocentric radius,  $h$  is the scale-length,  $z$  is height above the plane, and  $z_0$  is the scale-height of the disk.

To collapse Figure 23, we weight the volume densities with the exponential part of this equation since we aim to infer the vertical structure first, i.e., we assume a single scale-length and calculate  $\exp(-R/h)$  as a weight for each dwarf volume density. In Figure 24, the volume densities have all been scaled this way, assuming the scale-length ( $h$ ) of the thin disk from Jurić et al. (2008) of 2.6 kpc. They found a scale-length for the thick disk of  $h=2.9$  kpc. Alternatively, Bensby et al. (2011) found a thin-disk scale-length of  $h=3.8$  kpc and  $h=2.0$  for the thick disk, corroborated by Cheng et al. (2012) and the trend of stellar population and scale-length in Bovy et al. (2012). We use the Bensby et al. thin disk scale-length for dwarfs found in below 500 pc and the thick disk one for those more than 500 pc out of the plane. The implicit assumption in this renormalization is that the scale-height does not change with radius, which is observed in external galaxies seen edge-on (Comerón et al. 2011c,b,a, Streich et al *in preparation*).

Figure 24 shows more clearly how the later-type M-dwarfs (M4-8) in the BoRG fields are concentrated in the thin disk and the earlier types (M0-3) probe both thin and thick disks. It also shows that there may be several disk components in early types with different scale-heights above and below the plane of the disk. This would explain the North-South differential noted earlier by Pirzkal et al. (2009).

First we perform a naive fit on the vertical distribution of M-dwarfs as a function of sub-type: we fit the  $\operatorname{sech}^2(z/z_0)$  to their densities for each sub-type disregarding the different sampling or the existence more than a single disk component. Fit parameters,  $\rho_0$  and  $z_0$  are listed for each M-dwarf type in Table 10. The fit to the M4 dwarfs distribution is not a physical solution. Figure 25 shows the best fits to the densities and Figures 26 and 27, the central density and scale-height as a function of type.



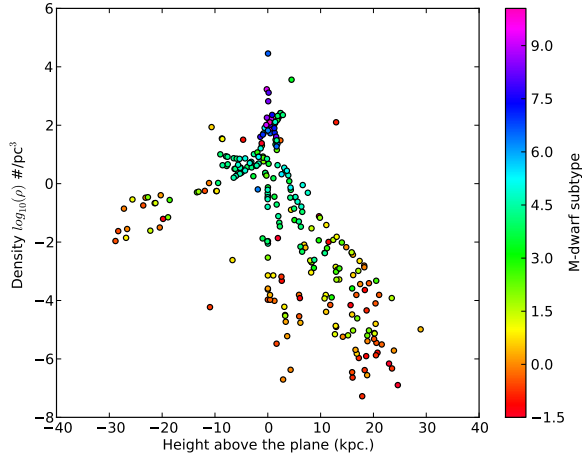


**Figure 24.** The volume density of M-dwarfs as a function as height above the plane of the Milky Way disk. The volume densities were normalized with a scale-length of 2.6 kpc. Points are color-coded by the M-dwarf sub-type.

The central densities in Figure 26 are not scaled by the central volume density of dwarfs. For comparison, we plot the volume densities computed from the local number of M-dwarfs compiled in Reid et al. (2008), their Figure 7, which is based on the numbers reported in Reid et al. (2004, 2007) and Cruz et al. (2007) for the latest M-dwarf types (M7-10). Table 9 lists the local densities as a function of M-dwarf type. We only note that both stay relatively constant with M-dwarf subtype.

Figure 27 shows the dependence of scale-height,  $z_0$  with M-dwarf subtype. The progressive decline in scale-height with subtype is in part due to the different heights sampled. Early types are a mix of thin and thick disk while later types were only found in the thin disk.

Bovy et al. (2012) argue that the different metallicities (and hence age) populations of the Milky Way all have their own distinct and unique scale-length and -height. They find that older populations are more concentrated (shorter scale-length) but the most vertically distributed (greatest scale-height). Similar results were found by Bensby et al. (2011) (using a thin/thick disk terminology) and Cheng et al. (2012). The trend between scale-height and M-dwarf subtype in Figure 27 fits with this general picture that there are not distinct thick and thin disks but a gradual transition in scales with stellar population. Because the majority of our fields are high Galactic latitude, we lack the statistics to perform a double fit (vertical and radial). We note however, that our use of the Bensby et al. (2011) thick- and thin-disk scale-lengths improved the vertical fits substantially over a single scale-length solution.

There are several “spurs” of stars in the height-density plot of Figure 25. To investigate if these correspond to specific areas in the Milky Way, we replot the height-density plot for all M-dwarfs, coded with the Galactic position in Figure 28. Substructures become visible as a function of Galactic Longitude. For example, the upturn in M-dwarfs at 0 to -10 kpc above the plane is due to a few fields near  $l \geq 310^\circ$  and  $b = -40^\circ$ . The Longitude position strongly suggests the Milky Way Bulge as

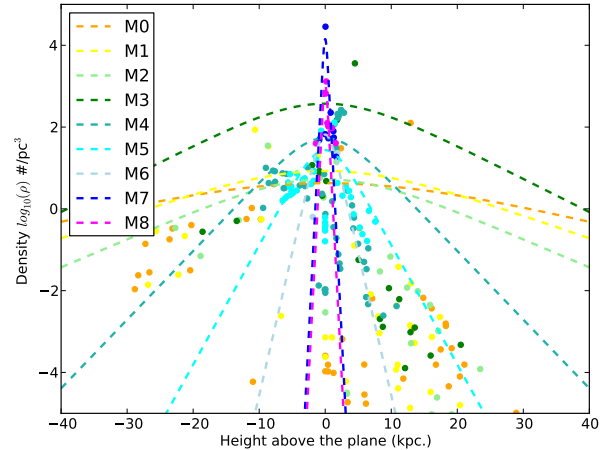


**Figure 25.** The volume density of M-dwarfs as a function as height above the plane of the Milky Way disk. Points are grayscale-coded by the M-dwarf sub-type with best fits shown for each M-dwarf type.

**Table 10**

The vertical profile fits to the full sample of identified M-dwarfs.

M-type (o)	$\rho_0$ (#/pc <sup>3</sup> )	$z_0$ (kpc)
0	4.25	$22.85 \pm 32.92$
1	8.44	$15.50 \pm 14.33$
2	5.29	$12.62 \pm 9.22$
3	373.12	$10.69 \pm 14.41$
4	53.93	$-5.17 \pm 2.74$
5	27.27	$2.97 \pm 1.39$
6	65.78	$1.24 \pm 0.42$
7	14185.51	$0.28 \pm 0.41$
8	1066.36	$0.28 \pm 0.12$

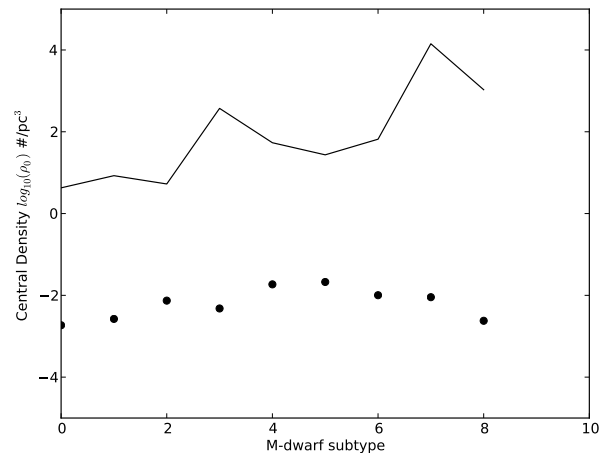


**Figure 26.** The central density of the best fit as a function of the M-dwarf type. The black circles are the values from Reid et al. (2008).

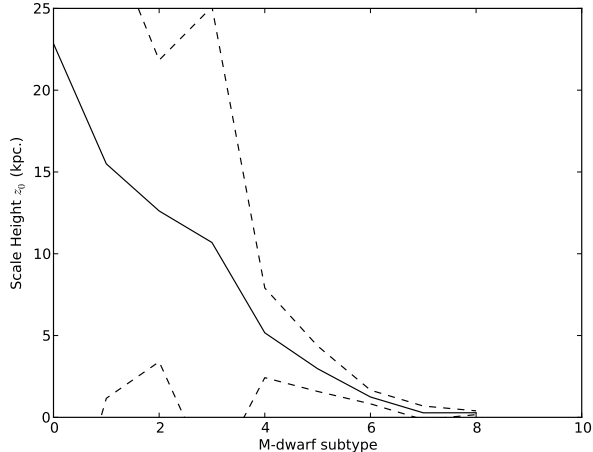


**Figure 27.** The scale-height of the best fit as a function of the M-dwarf type. Dashed lines are the uncertainty in the fit.

the origin of the additional M-dwarfs but the Latitude is quite low for much of the effect of the Galactic bulge.

To characterize the different scale-heights implied by the spurs in Figure 28, we selected Galactic longitude or latitude sections for a  $sech^2$  fit, summarized in Tables 11 and 12. The  $sech^2$  fits to these cuts show an expected variety of  $z_0$  values. Given the vertical extent that the observations probe, contributions from stellar halo components are likely included (similar to the Sagittarius stream in §6.2). For example, the spur of stars at 20 kpc at  $l = -75^\circ$  and  $b = -75^\circ$  (yellow and red points in Figure 28 left and right panel respectively) is at a higher density than one would expect from the different Latitude observations at  $l = 120^\circ$  (green point in Figure 28, left panel). However, that spur is the result of a single field and this may be simple cosmic variance in our counts. To reliably detect halo substructure or even typical scales, using M-dwarfs, one needs to image a much greater area of sky continuously (i.e., with EUCLID).

**Table 11**

The fits to selected Galactic Latitude cuts.

$b$ ( $^\circ$ )	$\rho_0$ ( $\#/pc^3$ )	$z_0$ (kpc)
-75.00	140.03	$0.77 \pm 0.00$
-55.00	60.60	$2.14 \pm 0.07$
10.00	451455.50	$0.02 \pm 0.01$
35.00	2394.64	$0.19 \pm 0.00$
52.00	172.83	$1.48 \pm 0.27$
60.00	25.13	$1.98 \pm 0.01$

#### 6.4. L and T Dwarfs

We do find a number of stellar objects in the L and T color selection criteria from Ryan et al. (2011). There is one object, brighter than 24 mag in  $F125W$  in these fields that fall into the T-dwarf box. This is not the sole T-dwarf identified by Ryan et al. (2011) which is a 25.08 mag object. Table 15 lists the properties of the single  $m < 24$ T-dwarf stars in BoRG. The color-color selection

**Table 12**

The fits to selected Galactic Longitude cuts.

$l$ ( $^\circ$ )	$\rho_0$ ( $\#/pc^3$ )	$z_0$ (kpc)
310.00	6.45	$6.68 \pm 0.38$
235.00	716.35	$0.28 \pm 0.00$
75.00	12.64	$32.24 \pm 77.73$
85.00	1921.33	$0.54 \pm 0.00$
120.00	3875.14	$0.13 \pm 0.01$
140.00	12.58	$3.84 \pm 3.12$

also identifies 30 L-dwarfs in the BoRG survey. Table 16 lists their properties. Neither T nor L dwarfs have a reasonably well-calibrated relation between optical-near infrared color and sub-type (see e.g., Burningham et al. 2013) to allow for a distance estimate similar to the M-dwarfs, nor do we have the statistics in hand to infer a scale-height for these objects.

Wilkins et al. (2014) reiterate that L and T-dwarfs pose a risk of contaminating high redshift ( $z \sim 7$ ) color-selected samples and show how some dwarf spectra may even masquerade as objects with emission lines. They generated their color selections similar to Ryan et al. (2011) and the boxes in Figure 12 do generally agree with the derived colors. Wilkins et al. (2014) claim HST morphological information is insufficient to cull L- and T-dwarfs from a high-redshift galaxy sample. We have shown that dwarfs can be unequivocally identified by their stellar morphology using simple tools such as SEXTRACTOR down to 24. AB mag in *undithered* WFC3 data and a reliably star/galaxy separation is not only crucial for high-redshift studies but very likely possible down to much lower luminosities. The second issue is the surface density of these later dwarf types. For the first time, we can give an indication for random high-latitude, space-based observations based on the number of L-dwarfs found (Table 16). Figure 29 shows the surface density of L-dwarfs selected by our morphology and color criteria. It shows a WFC3 exposure has  $< 1$  L-dwarf that can be selected against morphologically. Extrapolating to lower luminosities (including improved star/galaxy separation), the contamination problem may not be as dire as predicted. For example, Wilkins et al. (2014) assume that the local brown dwarf density ( $0.015$  stars/ $pc^3$ ) holds throughout all the Milky Way components (thin and thick disks and halo). However, the spatial density drops exponentially with height above the plane. If L- and T-dwarfs follow a similar scale-height as the M-dwarfs examined here ( $z_0 \sim 300$  pc), then contaminating dwarf stars at 1-2 kpc distance will be very rare, even before morphological selection.

## 7. CONCLUSIONS

- Stars can be selected best using SEXTRACTOR's half-light radius ( $r_{50}$ ), corroborating previous identifications (Figures 8 and 17).
- M-dwarfs can be reliably sub-typed using a near-infrared and optical color (Figure 14).
- Relatively more early-type M-dwarfs are identified in Northern fields as opposed to Southern Galactic

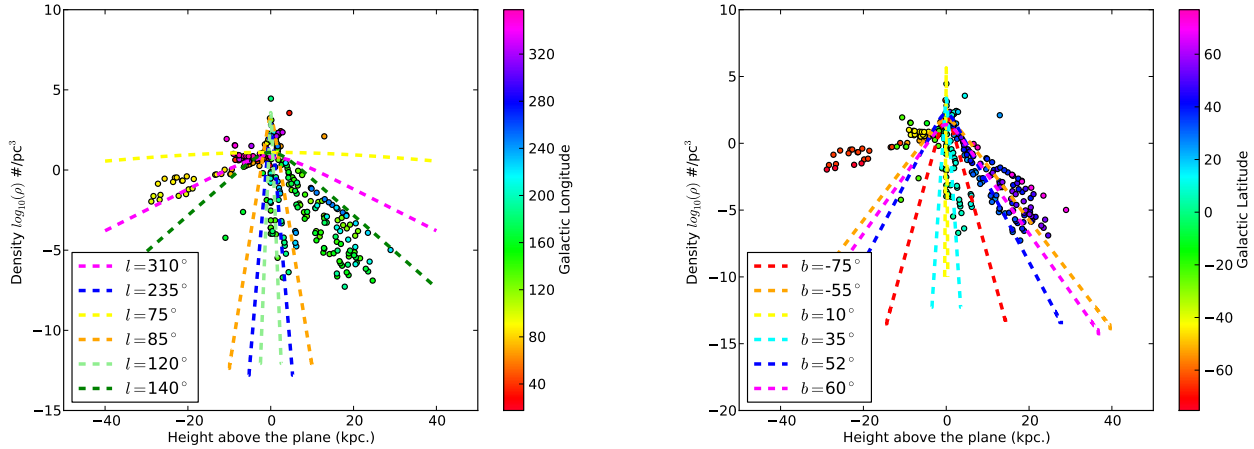


**Figure 28.** The volume density of M-dwarfs as a function as height above the plane of the Milky Way disk. Points are color-coded by the dwarf’s Galactic Longitude (left) and Latitude (right panel).

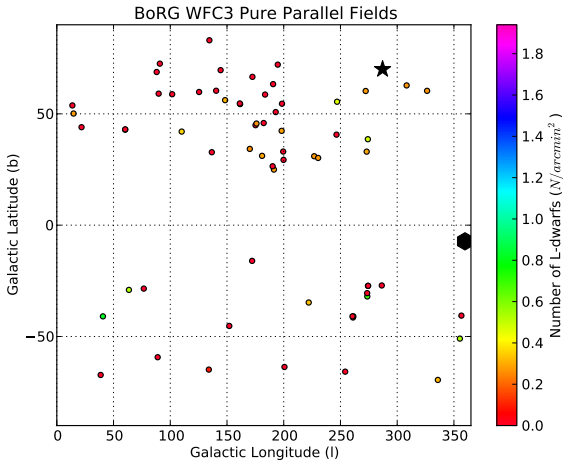


**Figure 29.** The distribution of BoRG fields with the number of L-dwarfs indicated. Other symbols identical to Figure 21.

ones. This confirms the dichotomy Pirzkal et al. (2009) noted (Table 8).

- We report an over-density in one of our fields, borg\_1230+0750, consistent with the M-dwarf members of the Sagittarius stream at a distance of 20-25 kpc. (Figure 22).
- A naive, single-component fit of the vertical distribution of M-dwarfs shows a steady decline of scale-height,  $z_0$ , with M-dwarf sub-type (Figure 27).
- The grouping of spurs of stars at different Galactic coordinates strongly hints at substructure in the Milky Way disk/halo of M-dwarfs (Figure 28).

## 8. FUTURE WORK

Future work with WFC3 (pure-parallel) programs on Milky Way Dwarfs will use the ever-increasing number of sight-lines available to build a comprehensive catalog of M,L and T dwarfs belonging to the thin and thick disks and stellar halo of our Milky Way. New pure-parallel

observational programs with HST/WFC3 are needed to expand the number of sight-lines and improve statistics. At lower Galactic latitudes, this could easily be achieved with lower integration times than the BoRG or HIPPIES programs. Once such a proposed program is completed fully, the total tally of M-dwarfs should give a first idea of the size and shape of the Milky Way disks, thin and thick, and depending on the total statistics, the Galactic Halo.

In parallel, spectroscopic identification of Milky Way dwarf stars by the HST-3D near-infrared grism spectra (e.g., Brammer et al. 2012). The ongoing imaging and grism campaigns on the CANDELS fields (Koeke-moer et al. 2011; Grogin et al. 2011) will improve the calibration of the photometric identifications of Galactic Dwarfs in the pure-parallel surveys as well as add additional statistics to the star counts.

The general technique of morphologically identifying stars in space-based imaging, identifying dwarfs from near-infrared colors and subsequently sub-type these using an optical-near-infrared color will be perfectly suited for the EUCLID mission (Laureijs et al. 2011). The wide-band optical filter can be used to morphologically identify the stars and the three near-infrared filters to hone in on the Galactic dwarfs. Finally, the optical-nir color and complementary grism spectroscopy can then be used to subtype these dwarfs. With the wide survey area to faint point source sensitivity (all-sky 24 mag, 26 mag in deep fields) the EUCLID mission will yield an accurate measure of the shape and size of our Milky Way in sub-solar dwarfs as well as an accurate census of Halo substructure similar to the Sagittarius stream. Limiting factors may be the PSF in the near-infrared, leading to confusion issues and the width of the optical filter complicating subtyping. However, the two independent-angle grism spectra of all the objects in the field should unequivocally identify the Galactic dwarf stars.

Milky Way dwarfs are unlikely to be the focus of James Webb Space Telescope observations but they will certainly feature in them. The ubiquity of M-dwarfs in the BoRG fields points to their possible use as fine guidance for JWST image and NIRspec imaging/MOS registra-

tion.

The authors would like to thank N. Reid and K. Cruz for their help with the local density of M-dwarfs and R. Benjamin for useful discussions on Galactic substructures. The lead author thanks the European Space Agency for the Fellowship program and its support. We acknowledge the support of HST Archival grant number AR-12134, General Observer Grants GO-11700, GO-12572, and GO-12905 and the European Space Agency for support of this work. MT was partially supported by the European Commission through the Marie Curie Career Integration Fellowship PCIG12-GA-2012-333749. This work is based in part on observations taken by the CANDELS Multi-Cycle Treasury Program with the NASA/ESA HST, which is operated by the Association of Universities for Research in Astronomy, Inc., under NASA contract NAS5-26555. This research has made use of the NASA/IPAC Extragalactic Database (NED) which is operated by the Jet Propulsion Laboratory, California Institute of Technology, under contract with the National Aeronautics and Space Administration. This research has made use of NASA's Astrophysics Data System.

#### REFERENCES

- Bahcall, J. N. 1986, *ARA&A*, 24, 577  
 Beckwith, S. V. W. et al. 2006, *AJ*, 132, 1729  
 Belokurov, V. et al. 2013, *ArXiv e-prints*  
 —. 2006, *ApJ*, 642, L137  
 Bensby, T. et al. 2011, *ApJ*, 735, L46  
 Bertin, E., & Arnouts, S. 1996, *A&AS*, 117, 393, provided by the NASA Astrophysics Data System  
 Bochanski, J. J. et al. 2013, *ArXiv e-prints*  
 Bovy, J. et al. 2012, *ApJ*, 753, 148  
 Bradley, L. D. et al. 2012, *ApJ*, 760, 108  
 Brammer, G. et al. 2012, *ArXiv e-prints*  
 Burningham, B. et al. 2013, *ArXiv e-prints*  
 Caballero, J. A. et al. 2008, *A&A*, 488, 181  
 Casertano, S. et al. 2000, *AJ*, 120, 2747  
 Cheng, J. Y. et al. 2012, *ApJ*, 752, 51  
 Comerón, S. et al. 2011a, *ApJ*, 741, 28  
 —. 2011b, *ApJ*, 738, L17  
 —. 2011c, *ApJ*, 729, 18  
 Cruz, K. L. et al. 2007, *AJ*, 133, 439  
 Dressel, L. et al. 2010, in *Wide Field Camera 3 Instrument Handbook*, Version 3.0  
 Fruchter, A. S., & Hook, R. N. 2002, *PASP*, 114, 144  
 Gialalisco, M. et al. 2004, *ApJ*, 600, L93  
 Gilmore, G. 1984, *MNRAS*, 207, 223  
 Gilmore, G., & Reid, N. 1983, *MNRAS*, 202, 1025  
 Gilmore, G. et al. 1989, *ARA&A*, 27, 555  
 Grogin, N. A. et al. 2011, *ApJS*, 197, 35  
 Hawley, S. L. et al. 2002, *AJ*, 123, 3409  
 Holwerda, B. W. 2005, *astro-ph/0512139*  
 Holwerda, B. W. et al. 2005, *AJ*, 129, 1396  
 Jurić, M. et al. 2008, *ApJ*, 673, 864  
 Kapteyn, J. C. 1922, *ApJ*, 55, 302  
 Kilic, M. et al. 2005, *ApJ*, 633, 1126  
 King, I. et al., eds. 1990, *The Milky Way As Galaxy*  
 Koekemoer, A. M. et al. 2011, *ApJS*, 197, 36  
 Laureijs, R. et al. 2011, *ArXiv e-prints*  
 Leauthaud, A. et al. 2007, *ApJS*, 172, 219  
 Majewski, S. R. 1993, *ARA&A*, 31, 575  
 Majewski, S. R. et al. 2003, *ApJ*, 599, 1082  
 Newberg, H. J. et al. 2002, *ApJ*, 569, 245  
 Pirzkal, N. et al. 2009, *ApJ*, 695, 1591  
 —. 2005, *ApJ*, 622, 319  
 —. 2004, *ApJS*, 154, 501  
 Reid, I. N. et al. 2004, *AJ*, 128, 463  
 —. 2007, *AJ*, 133, 2825  
 —. 2008, *AJ*, 136, 1290  
 Ryan, R. E. et al. 2011, *ApJ*, 739, 83  
 Ryan, Jr., R. E. et al. 2005, *ApJ*, 631, L159  
 Siegel, M. H. et al. 2002, *ApJ*, 578, 151  
 Stanway, E. R. et al. 2008, *MNRAS*, 384, 348  
 Steidel, C. C. et al. 1996, *AJ*, 112, 352  
 Trenti, M. et al. 2011, *ApJ*, 727, L39  
 —. 2012, *ApJ*, 746, 55  
 Trenti, M., & Stiavelli, M. 2008, *ApJ*, 676, 767  
 van Dokkum, P. G. 2001, *PASP*, 113, 1420  
 Widrow, L. M. et al. 2012, *ArXiv e-prints*  
 Wilkins, S. M. et al. 2014, *ArXiv e-prints*  
 Windhorst, R. A. et al. 2011, *ApJS*, 193, 27  
 Yan, H. et al. 2010, *ArXiv e-prints*  
 Yanny, B., & Gardner, S. 2013, *ArXiv e-prints*  
 Zheng, Z. et al. 2001, *ApJ*, 555, 393

**Table 13**  
Basic Data for the BoRG fields of the second data release from Bradley et al. (2012) and Schmidt et al. *in preparation*.

Field	Exptime (sec.)	Area amin <sup>2</sup>	RA J2000	DEC J2000	<i>l</i> o	<i>b</i> o	zp mag	<i>zP<sub>fin</sub></i> mag	Lim Mag	E(B-V)	<i>A<sub>F098M</sub></i>	<i>A<sub>F125W</sub></i>	<i>A<sub>F160W</sub></i>	<i>A<sub>F606W</sub></i>	<i>A<sub>F600LP</sub></i>
borg_0110-0224	1358.2	10.9	17.531664	-2.395226	133.978373	-64.865306	26.2	26.2	26.9	0.046	0.060	0.041	0.029	0.140	0.104
borg_0214+1255	1402.9	3.8	33.409984	12.915292	152.017084	-45.263536	26.2	26.1	25.9	0.122	0.158	0.109	0.077	...	0.273
borg_0228-4102	1402.9	3.7	36.906588	41.025888	254.161019	-65.793327	26.2	26.2	26.8	0.015	0.019	0.013	0.009	...	0.033
borg_0240-1857	1402.9	3.6	40.114070	-18.953931	200.647911	-63.687697	26.2	26.2	26.7	0.033	0.043	0.030	0.021	...	0.074
borg_0427+2538	702.9	4.3	66.690208	25.640444	172.153535	-16.034094	26.2	25.4	25.1	0.906	1.173	0.809	0.574	...	2.031
borg_0436-5259	2905.9	3.2	69.059214	-52.986412	261.052355	-41.464289	26.2	26.2	27.3	0.007	0.009	0.006	0.004	...	0.015
borg_0439-5317	3005.9	3.3	69.855420	-53.278154	261.335374	-40.946634	26.2	26.2	27.2	0.005	0.006	0.004	0.003	...	0.011
borg_0440-5244	2002.9	3.4	69.958786	-52.731210	260.606945	-40.966425	26.2	26.2	27.0	0.006	0.008	0.006	0.004	...	0.014
borg_0540-6409	2308.8	1.4	84.879133	-64.150953	273.650789	-32.015266	26.2	26.2	26.6	0.057	0.074	0.051	0.036	...	...
borg_0553-6405	2611.7	1.7	88.275723	-64.088263	273.525627	-30.535388	26.2	26.2	26.8	0.045	0.059	0.040	0.029	...	...
borg_0624-6432	1205.9	3.2	95.897657	-64.528319	274.231122	-27.261687	26.2	26.2	26.4	0.058	0.075	0.052	0.037	...	...
borg_0624-6440	1205.9	3.2	95.950899	-64.662581	274.384073	-27.253871	26.2	26.2	26.6	0.059	0.076	0.053	0.037	...	...
borg_0637-7518	2411.7	5.0	99.265244	-75.312608	286.420817	-27.079824	26.2	26.2	26.6	0.101	0.131	0.090	0.064	...	...
borg_0751+2917	5114.7	3.5	117.709478	29.281998	191.357531	24.959335	26.2	26.2	27.1	0.043	0.055	0.038	0.027	...	0.096
borg_0756+3043	1905.9	3.3	118.988521	30.717701	190.217249	26.453514	26.2	26.2	26.6	0.062	0.081	0.056	0.040	...	...
borg_0808+3946	2205.9	3.4	122.089304	39.758799	180.921586	31.128951	26.2	26.2	26.6	0.045	0.059	0.040	0.029	...	...
borg_0819+4911	1205.9	3.9	124.830368	49.183970	170.094798	34.245407	26.2	26.2	26.5	0.051	0.066	0.046	0.032	...	...
borg_0820+2332	702.9	3.7	125.013578	23.535374	199.823057	29.325880	26.2	26.2	26.1	0.045	0.058	0.040	0.029	...	...
borg_0835+2456	2205.9	3.7	128.820679	24.936409	199.532045	33.060979	26.2	26.2	26.7	0.030	0.039	0.027	0.019	...	...
borg_0846+7654	2002.9	3.4	131.592805	76.893333	136.609253	32.760391	26.2	26.2	26.2	0.023	0.030	0.021	0.015	...	0.052
borg_0906+0255	2708.8	3.6	136.405132	2.925182	226.847796	30.959816	26.2	26.2	27.0	0.031	0.040	0.027	0.019	...	...
borg_0909+0002	1805.9	3.6	137.286275	-0.029911	230.317128	40.193272	26.2	26.2	26.7	0.031	0.032	0.027	0.019	...	...
borg_0914+2822	2205.9	3.5	138.569416	28.361907	198.147524	42.355253	26.2	26.2	26.8	0.025	0.030	0.022	0.016	...	...
borg_0922+4505	2105.9	3.7	140.406384	45.087611	175.139682	44.898070	26.2	26.2	26.5	0.020	0.026	0.018	0.013	...	...
borg_0926+4000	1105.9	4.0	141.392945	40.005560	182.318366	45.875115	26.2	26.2	26.2	0.015	0.020	0.014	0.010	...	...
borg_0926+4426	1602.9	3.7	141.382123	44.426101	175.988847	45.646771	26.2	26.2	26.7	0.016	0.020	0.014	0.010	...	0.035
borg_1010+3001	3211.7	3.8	152.405996	30.018416	198.478129	54.538030	26.2	26.2	26.8	0.024	0.032	0.022	0.015	...	...
borg_1014-0423	1105.9	3.3	153.523466	-4.378731	246.512301	40.637070	26.2	26.2	26.2	0.036	0.046	0.032	0.023	...	0.080
borg_1031+3804	1505.9	3.8	157.715302	38.058891	183.562795	58.661992	26.2	26.2	26.3	0.014	0.018	0.012	0.009	...	...
borg_1031+5052	4811.7	4.4	157.690654	50.861755	161.556783	54.378702	26.2	26.2	27.1	0.011	0.015	0.010	0.007	...	...
borg_1033+5051	3211.7	4.5	158.212380	50.859570	161.288017	54.668744	26.2	26.2	26.8	0.015	0.020	0.014	0.010	...	...
borg_1051+3359	3317.6	3.2	162.822134	33.985372	190.638764	63.346845	26.2	26.2	27.0	0.026	0.033	0.023	0.016	...	...
borg_1103-2330	4411.7	3.5	165.807563	-23.506099	273.102916	33.023056	26.2	26.2	27.2	0.063	0.082	0.056	0.040	...	...
borg_1111+5545	2605.9	3.2	167.736508	55.750992	148.327174	56.140872	26.2	26.2	27.0	0.017	0.022	0.015	0.011	...	...
borg_1119+4026	1402.9	3.7	169.513804	40.397987	172.408816	66.608159	26.2	26.2	26.8	0.016	0.020	0.014	0.010	...	0.035
borg_1131+3114	1402.9	3.7	172.876206	31.289335	194.731674	72.096104	26.2	26.2	26.8	0.023	0.029	0.020	0.014	...	...
borg_1152+5441	2808.8	3.5	177.958339	54.684118	140.431973	60.372656	26.2	26.2	27.1	0.010	0.013	0.009	0.006	...	...
borg_1153+0056	2208.8	3.6	178.182290	0.931268	272.226679	60.255130	26.2	26.2	26.7	0.022	0.028	0.019	0.014	...	...
borg_1209+4543	3708.8	3.6	182.354635	45.723905	144.365550	69.616030	26.2	26.2	27.2	0.014	0.018	0.013	0.009	...	...
borg_1230+0750	1805.9	0.5	187.469950	7.825175	287.119671	70.032220	26.2	26.2	26.0	0.024	0.031	0.021	0.015	...	0.021
borg_1242+5716	2508.8	3.5	190.553698	57.270437	125.411526	59.813474	26.2	26.2	26.9	0.009	0.012	0.008	0.006	...	...
borg_1245+3356	1505.9	3.8	191.186033	33.935834	134.469175	83.041931	26.2	26.2	26.7	0.016	0.021	0.015	0.010	...	0.049
borg_1301+0000	1602.9	3.7	195.317726	-0.007321	308.309140	62.761637	26.2	26.2	26.1	0.025	0.033	0.023	0.016	...	0.057
borg_1337+0228	1202.9	3.7	204.202249	-0.463529	326.341939	60.329542	26.2	26.2	26.6	0.030	0.039	0.027	0.019	...	0.067
borg_1341+4123	3205.9	3.3	205.130683	41.384472	90.818133	72.544121	26.2	26.2	27.2	0.007	0.009	0.006	0.004	...	0.015
borg_1408+5503	2611.8	3.5	211.992568	55.055640	101.682613	58.802067	26.2	26.2	26.9	0.014	0.018	0.012	0.009	...	...
borg_1437+5043	2508.8	3.6	219.233553	50.718933	89.759393	59.068028	26.2	26.2	27.0	0.013	0.016	0.011	0.008	...	...
borg_1524+0954	1602.9	3.5	231.040910	9.905686	14.750963	50.138306	26.2	26.2	26.5	0.042	0.055	0.038	0.027	...	0.095
borg_1555+1108	2908.8	3.4	238.856610	11.131677	271.91448	44.001085	26.2	26.2	27.0	0.052	0.068	0.047	0.033	...	...
borg_1632+3733	2405.9	3.5	248.074403	37.557004	60.247231	42.879109	26.2	26.2	27.0	0.010	0.014	0.009	0.007	...	...
borg_1632+3737	1205.9	3.5	247.891785	37.608886	60.304175	43.027091	26.2	26.2	26.6	0.010	0.013	0.009	0.006	...	...
borg_2057-4412	1202.9	3.5	314.340154	-44.206786	356.583873	-40.623775	26.2	26.2	26.4	0.038	0.049	0.034	0.024	...	0.085
borg_2132+1004	1005.9	3.8	323.061958	10.063711	63.564901	-29.075332	26.2	26.2	26.4	0.040	0.052	0.036	0.026	...	0.090
borg_2155-4411	1402.9	3.7	328.812024	-44.176682	355.248970	-50.945449	26.2	26.2	26.7	0.013	0.016	0.011	0.008	...	0.028
borg_2203+1851	2005.9	3.4	330.704916	18.850050	76.655821	-28.494164	26.2	26.2	26.8	0.069	0.090	0.062	0.044	...	0.155
borg_2345+0054	1402.9	3.8	356.260909	-0.901806	88.898069	-59.313470	26.2	26.2	26.8	0.036	0.047	0.033	0.023	...	0.082
borg_2351-4332	4208.8	3.1	357.650020	-43.525127	335.847122	-69.508926	26.2	26.2	27.3	0.013	0.017	0.011	0.008	...	0.029



**Table 13**  
 – *continued.* (BORG13) fields from Schmidt et al. *in preparation.*

Field	Exptime (sec.)	Area amin <sup>2</sup>	RA J2000	DEC J2000	<i>l</i> o	<i>b</i> o	zp mag	<i>zP<sub>fin</sub></i> mag	Lim Mag	E(B-V)	<i>A<sub>F098M</sub></i>	<i>A<sub>F125W</sub></i>	<i>A<sub>F160W</sub></i>	<i>A<sub>F606W</sub></i>	<i>A<sub>F600LP</sub></i>
borg_0456-2203	1809.0	3.1	73.964600	-22.048900	222.025278	-34.734134	26.2	26.3	26.7	0.038	0.037	0.028	0.020	0.095	...
borg_0951+3304	2212.0	1.8	147.700300	33.073700	192.933397	50.779624	26.2	26.3	26.5	0.013	0.013	0.010	0.007	0.033	...
borg_1059+0519	1806.0	2.1	164.703900	5.312500	247.014633	55.439033	26.2	26.3	26.8	0.028	0.027	0.020	0.014	0.070	...
borg_1118-1858	6276.0	2.0	169.410100	-18.972600	274.146911	38.600114	26.2	26.3	27.2	0.050	0.048	0.036	0.026	0.124	...
borg_1358+4334	3812.0	2.7	209.463600	43.561000	88.017132	68.790121	26.2	26.3	27.3	0.007	0.006	0.005	0.003	0.016	...
borg_1459+7146	2812.0	2.8	224.750100	71.763800	110.071478	42.032640	26.2	26.3	27.0	0.027	0.026	0.019	0.014	0.067	...
borg_1510+1115	9529.0	1.8	227.537100	11.241500	13.735263	53.779237	26.2	26.3	27.7	0.046	0.045	0.033	0.024	0.115	...
borg_2132-1202	1809.0	1.2	322.946700	-12.039700	40.659355	-40.966360	26.2	26.3	26.2	0.062	0.060	0.045	0.032	0.153	...
borg_2313-2243	6326.0	3.3	348.232600	-22.725200	38.654403	-67.276574	26.2	26.3	27.1	0.026	0.025	0.019	0.013	0.065	...

Table 14  
The 274 M-dwarfs identified in BoRG.

ID	ra	dec	l	b	$m_{F098M}$	$m_{F125W}$	$m_{F125W}$	$m_{F606W}$	Mtype	modulus	dist	Height	Radius
borg_0110-0224.551.0	17.501759	-2.418265	17.501759	-2.418265	23.8 ± 0.0	23.5 ± 0.0	23.3 ± 0.0	25.2 ± 0.1	-0.0 ± 0.2	16.48	19.74	-0.81	27.33
borg_0110-0224.719.0	17.503586	-2.415663	17.503586	-2.415663	24.3 ± 0.1	24.0 ± 0.0	23.9 ± 0.0	25.8 ± 0.0	5.1 ± 1.0	16.73	22.16	-0.91	29.63
borg_0110-0224.820.0	17.528020	-2.411389	17.528020	-2.411389	19.7 ± 0.0	19.5 ± 0.0	19.4 ± 0.0	22.8 ± 0.0	0.6 ± 0.2	8.59	0.52	0.01	9.00
borg_0110-0224.1016.0	17.553100	-2.408888	17.553100	-2.408888	24.5 ± 0.1	23.9 ± 0.0	23.7 ± 0.0	25.4 ± 0.1	6.0 ± 0.7	17.18	27.26	-1.12	34.49
borg_0110-0224.1414.0	17.559120	-2.400783	17.559120	-2.400783	24.1 ± 0.1	23.7 ± 0.1	23.4 ± 0.0	24.4 ± 0.1	11.6 ± 0.2	17.26	28.31	-1.16	35.49
borg_0110-0224.1529.0	17.564067	-2.398369	17.564067	-2.398369	24.2 ± 0.1	23.9 ± 0.0	23.8 ± 0.1	25.8 ± 0.2	2.0 ± 0.3	16.67	21.59	-0.88	29.08
borg_0110-0224.2048.0	17.516425	-2.384891	17.516425	-2.384891	22.8 ± 0.0	22.2 ± 0.0	22.2 ± 0.0	24.4 ± 0.0	5.8 ± 0.4	15.23	11.11	-0.44	19.09
borg_0110-0224.2599.0	17.523929	-2.371366	17.523929	-2.371366	22.3 ± 0.0	22.2 ± 0.0	22.1 ± 0.0	23.5 ± 0.0	2.6 ± 0.5	15.46	12.33	-0.48	20.26
borg_0110-0224.2683.0	17.528492	-2.352761	17.528492	-2.352761	24.4 ± 0.1	23.8 ± 0.0	23.5 ± 0.0	26.1 ± 0.2	-0.5 ± 0.3	15.47	12.40	-0.48	20.32
borg_0110-0224.3274.0	17.527112	-2.365442	17.527112	-2.365442	21.5 ± 0.0	21.2 ± 0.0	20.9 ± 0.0	23.0 ± 0.0	7.3 ± 0.0	14.22	6.99	-0.26	15.16
borg_0214+1255.93.0	33.407160	12.901716	33.407160	12.901716	23.4 ± 0.0	23.2 ± 0.0	23.0 ± 0.0	25.4 ± 0.0	5.5 ± 0.3	14.85	9.32	2.11	16.28
borg_0214+1255.129.0	33.404463	12.904437	33.404463	12.904437	23.8 ± 0.1	23.5 ± 0.0	23.5 ± 0.1	25.9 ± 0.9	-3.7 ± 0.1	15.13	10.64	2.40	17.38
borg_0214+1255.316.0	33.401479	12.914641	33.401479	12.914641	22.7 ± 0.0	22.3 ± 0.0	22.1 ± 0.0	24.5 ± 0.9	1.5 ± 0.2	13.94	6.15	1.40	13.63
borg_0214+1255.423.0	33.403924	12.919581	33.403924	12.919581	23.2 ± 0.0	23.0 ± 0.0	22.9 ± 0.0	25.3 ± 0.9	1.3 ± 0.2	14.66	8.56	1.94	15.65
borg_0214+1255.485.0	33.402208	12.932334	33.402208	12.932334	24.0 ± 0.1	23.7 ± 0.1	23.5 ± 0.1	25.9 ± 0.9	-2.3 ± 0.0	16.50	19.97	4.50	25.17
borg_0214+1255.527.0	33.401315	12.932255	33.401315	12.932255	23.7 ± 0.1	23.5 ± 0.0	23.4 ± 0.0	25.8 ± 0.9	0.7 ± 0.2	15.14	10.66	2.41	17.40
borg_0214+1255.675.0	33.419043	12.922374	33.419043	12.922374	22.1 ± 0.0	21.7 ± 0.0	21.4 ± 0.0	23.8 ± 0.9	-1.4 ± 0.3	14.49	7.90	1.79	15.09
borg_0228-4102.235.0	37.001751	-41.035498	37.001751	-41.035498	23.8 ± 0.0	23.7 ± 0.0	23.4 ± 0.0	26.0 ± 0.9	2.5 ± 0.6	15.37	11.88	-7.77	17.99
borg_0228-4102.356.0	36.962122	-41.031949	36.962122	-41.031949	23.0 ± 0.0	22.8 ± 0.0	22.8 ± 0.0	25.4 ± 0.9	-0.3 ± 0.2	13.40	4.79	-3.12	12.33
borg_0228-4102.975.0	36.995790	-41.013232	36.995790	-41.013232	24.4 ± 0.0	23.9 ± 0.0	23.8 ± 0.0	26.3 ± 0.9	2.8 ± 0.1	15.58	13.09	-8.56	18.95
borg_0240-1857.512.0	40.119316	-18.956384	40.119316	-18.956384	24.0 ± 0.0	23.7 ± 0.0	23.5 ± 0.0	26.0 ± 0.9	-3.3 ± 0.1	15.39	11.98	-3.86	17.66
borg_0240-1857.586.0	40.105209	-18.953743	40.105209	-18.953743	24.0 ± 0.0	23.2 ± 0.0	23.1 ± 0.0	25.6 ± 0.9	2.1 ± 0.0	14.89	9.50	-3.06	15.77
borg_0240-1857.630.0	40.105412	-18.952741	40.105412	-18.952741	24.0 ± 0.0	23.6 ± 0.0	23.6 ± 0.0	26.1 ± 0.9	-0.1 ± 0.2	14.19	6.89	-2.21	13.77
borg_0240-1857.696.0	40.114716	-18.950140	40.114716	-18.950140	23.3 ± 0.1	23.2 ± 0.1	23.2 ± 0.1	25.7 ± 1.0	0.5 ± 0.3	13.75	5.62	-1.80	12.80
borg_0240-1857.820.0	40.118697	-18.942101	40.118697	-18.942101	23.4 ± 0.0	23.1 ± 0.0	23.1 ± 0.0	25.6 ± 0.9	-3.3 ± 0.0	13.67	5.41	-1.73	12.64
borg_0240-1857.984.0	40.113448	-18.942479	40.113448	-18.942479	23.6 ± 0.0	23.5 ± 0.0	23.4 ± 0.0	26.0 ± 0.9	2.0 ± 0.1	14.08	6.55	-2.10	13.51
borg_0427+2538.267.0	66.667457	25.639670	66.667457	25.639670	24.1 ± 0.1	23.8 ± 0.1	23.5 ± 0.1	24.7 ± 1.0	-2.5 ± 0.1	17.37	29.83	12.93	20.31
borg_0427+2538.430.0	66.677165	25.645858	66.677165	25.645858	20.5 ± 0.0	20.1 ± 0.0	20.0 ± 0.0	21.2 ± 0.9	4.6 ± 0.1	13.68	5.45	2.39	10.66
borg_0436-5259.88.0	69.082749	-52.995795	69.082749	-52.995795	19.8 ± 0.0	19.6 ± 0.0	19.6 ± 0.0	22.1 ± 0.9	4.0 ± 0.7	10.14	1.07	-0.83	8.88
borg_0436-5259.1071.0	69.086775	-52.968191	69.086775	-52.968191	23.6 ± 0.0	23.4 ± 0.0	23.3 ± 0.0	25.3 ± 0.9	2.3 ± 0.1	13.93	6.11	-4.85	10.68
borg_0436-5259.1561.0	69.029594	-52.979986	69.029594	-52.979986	22.7 ± 0.0	22.3 ± 0.0	22.0 ± 0.0	24.6 ± 0.9	3.7 ± 0.1	13.96	6.18	-4.91	10.71
borg_0436-5259.1564.0	69.068430	-52.978812	69.068430	-52.978812	24.0 ± 0.0	23.8 ± 0.0	23.6 ± 0.0	26.2 ± 0.9	3.6 ± 0.1	14.31	7.29	-5.80	11.11
borg_0439-5317.47.0	69.842688	-53.294781	69.842688	-53.294781	23.6 ± 0.0	23.4 ± 0.0	23.3 ± 0.0	25.9 ± 0.9	4.4 ± 3.2	13.98	6.24	-4.98	10.65
borg_0439-5317.485.0	69.841510	-53.281842	69.841510	-53.281842	23.8 ± 0.0	23.5 ± 0.0	23.4 ± 0.0	26.0 ± 0.9	3.1 ± 0.1	14.10	6.62	-6.06	10.78
borg_0439-5317.490.0	69.858924	-53.275014	69.858924	-53.275014	24.1 ± 0.1	23.8 ± 0.1	23.8 ± 0.1	26.3 ± 0.9	3.2 ± 0.1	14.40	7.60	-5.02	11.12
borg_0440-5244.296.0	69.965551	-52.751075	69.965551	-52.751075	24.4 ± 0.0	23.7 ± 0.0	23.5 ± 0.0	26.0 ± 0.9	3.8 ± 0.1	15.37	11.85	-9.40	12.56
borg_0440-5244.1108.0	69.948227	-52.720162	69.948227	-52.720162	23.2 ± 0.0	23.1 ± 0.0	23.1 ± 0.0	25.7 ± 1.1	3.2 ± 0.1	13.68	5.44	-4.30	10.36
borg_0440-5244.1171.0	69.966089	-52.722258	69.966089	-52.722258	24.2 ± 0.0	24.0 ± 0.0	23.9 ± 0.0	26.5 ± 0.9	3.9 ± 0.1	14.55	8.15	-6.45	11.29
borg_0540-6409.359.0	84.878756	-64.166787	84.878756	-64.166787	23.3 ± 0.0	23.2 ± 0.0	23.2 ± 0.0	24.4 ± 0.1	3.4 ± 0.2	16.77	22.55	-20.27	10.51
borg_0540-6409.1388.0	84.915147	-64.157166	84.915147	-64.157166	23.7 ± 0.0	23.5 ± 0.1	23.5 ± 0.1	24.6 ± 0.1	4.0 ± 0.1	17.05	25.75	-23.14	10.78
borg_0540-6409.1795.0	84.848728	-64.153115	84.848728	-64.153115	22.6 ± 0.1	21.9 ± 0.0	21.8 ± 0.0	23.0 ± 0.0	3.4 ± 0.0	15.46	12.39	-11.12	9.61
borg_0540-6409.2227.0	84.917103	-64.151627	84.917103	-64.151627	24.2 ± 0.0	24.0 ± 0.0	23.9 ± 0.0	25.4 ± 0.2	4.7 ± 0.2	17.27	28.50	-25.62	11.02
borg_0540-6409.4029.0	84.839331	-64.142778	84.839331	-64.142778	24.1 ± 0.0	24.0 ± 0.0	24.0 ± 0.1	25.7 ± 0.2	4.0 ± 0.1	17.01	25.25	-22.69	10.77
borg_0553-6405.276.0	88.272416	-64.102643	88.272416	-64.102643	23.7 ± 0.0	23.1 ± 0.0	23.0 ± 0.0	25.0 ± 0.1	3.0 ± 0.0	15.87	14.94	-13.41	8.95
borg_0553-6405.417.0	88.272842	-64.100426	88.272842	-64.100426	22.5 ± 0.0	22.2 ± 0.0	21.9 ± 0.0	25.6 ± 0.2	3.8 ± 0.1	11.02	1.60	-1.41	8.55
borg_0553-6405.921.0	88.308827	-64.096097	88.308827	-64.096097	24.2 ± 0.0	23.8 ± 0.0	23.6 ± 0.0	25.7 ± 0.2	4.8 ± 0.1	16.58	20.68	-18.58	9.11
borg_0553-6405.1426.0	88.255567	-64.093062	88.255567	-64.093062	24.1 ± 0.0	23.9 ± 0.0	23.6 ± 0.0	25.0 ± 0.1	3.6 ± 0.1	17.41	30.30	-27.23	9.42
borg_0553-6405.1869.0	88.302676	-64.086143	88.302676	-64.086143	18.5 ± 0.0	18.4 ± 0.0	18.2 ± 0.0	22.2 ± 0.0	5.3 ± 0.1	6.93	0.24	-0.19	8.51
borg_0553-6405.1940.0	88.237113	-64.089216	88.237113	-64.089216	23.5 ± 0.0	23.3 ± 0.0	23.2 ± 0.0	24.1 ± 0.0	4.4 ± 0.1	16.89	23.84	-21.42	9.23
borg_0624-6440.377.0	95.901222	-64.514287	95.901222	-64.514287	24.5 ± 0.1	23.9 ± 0.0	23.8 ± 0.1	24.9 ± 0.1	3.9 ± 0.1	17.48	31.40	-28.31	5.27
borg_0624-6440.1500.0	95.959018	-64.672887	95.959018	-64.672887	23.3 ± 0.0	23.2 ± 0.0	23.1 ± 0.0	23.9 ± 0.0	3.9 ± 0.1	16.71	21.96	-19.83	6.22
borg_0624-6440.671.0	95.974795	-64.668131	95.974795	-64.668131	24.2 ± 0.1	23.8 ± 0.0	23.8 ± 0.1	24.9 ± 0.1	4.3 ± 0.1	17.35	29.49	-26.63	5.43
borg_0624-6440.855.0	95.965176	-64.668395	95.965176	-64.668395	21.3 ± 0.0	21.0 ± 0.0	21.0 ± 0.0	24.2 ± 0.1	4.6 ± 0.1	10.60	1.05	-0.93	8.39
borg_0624-6440.1530.0	95.947932	-64.647949	95.947932	-64.647949	23.7 ± 0.0	23.6 ± 0.0	23.4 ± 0.0	25.3 ± 0.1	4.3 ± 0.1	16.60	20.92	-18.88	6.33
borg_0637-7518.413.0	99.200816	-75.325023	99.200816	-75.325023	24.2 ± 0.0	23.9 ± 0.0	23.8 ± 0.1	25.3 ± 0.2	4.7 ± 0.3	17.22	27.76	-26.83	4.06
borg_0637-7518.860.0	99.274053	-75.315106	99.274053	-75.315106	23.3 ± 0.0	23.1 ± 0.0	23.0 ± 0.0	24.1 ± 0.1	4.7 ± 0.1	16.63	21.17	-20.45	5.09
borg_0637-7518.1385.0	99.310263	-75.302378	99.310263	-75.302378	18.7 ± 0.0	18.5 ± 0.0	18.3 ± 0.0	21.1 ± 0.0	3.5 ± 0.1	9.04	0.64	-0.59	8.40
borg_0637-7518.1339.0	99.346277	-75.306673	99.346277	-75.306673	24.3 ± 0.0	23.8 ± 0.0	23.7 ± 0.1	24.8 ± 0.1	4.5 ± 0.1	17.37	29.84	-28.83	3.65
borg_0637-7518.1477.0	99.348426	-75.296890	99.348426	-75.296890	20.4 ± 0.0	20.2 ± 0.0	20.2 ± 0.0	22.8 ± 0.0	5.2 ± 0.1	10.77	1.42	-1.35	8.27
borg_0637-7518.1698.0	99.295092	-75.297882	99.295092	-75.297882	23.7 ± 0.0	23.5 ± 0.0	23.4 ± 0.0	25.1 ± 0.1	-1.7 ± 0.1	16.81	23.02	-22.24	4.78





Table 14  
– continued

ID	ra	dec	l	b	$m_{F098M}$	$m_{F125W}$	$m_{F125W}$	$m_{F606W}$	Mtype	modulus	dist	Height	Radius
borg_1337+0028.119.0	204.215604	-0.477434	204.215604	-0.477434	23.2 ± 0.1	23.1 ± 0.0	23.0 ± 0.0	25.5 ± 0.9	-0.3 ± 0.5	13.62	5.30	-0.02	3.66
borg_1337+0028.242.0	204.190280	-0.4774715	204.190280	-0.4774715	23.0 ± 0.0	22.9 ± 0.0	22.8 ± 0.0	25.4 ± 0.9	0.5 ± 0.3	13.44	4.87	-0.01	4.06
borg_1337+0028.357.0	204.209496	-0.472242	204.209496	-0.472242	23.5 ± 0.0	23.3 ± 0.0	23.2 ± 0.0	25.8 ± 0.9	1.0 ± 1.9	13.82	5.82	-0.02	3.19
borg_1337+0028.816.0	204.215569	-0.463074	204.215569	-0.463074	24.1 ± 0.0	24.0 ± 0.0	23.7 ± 0.0	26.3 ± 0.9	2.2 ± 0.2	15.63	13.38	-0.08	-3.71
borg_1337+0028.845.0	204.184943	-0.460774	204.184943	-0.460774	23.9 ± 0.0	23.7 ± 0.0	23.7 ± 0.0	26.2 ± 0.9	1.9 ± 0.2	14.29	7.20	-0.03	1.93
borg_1337+0028.1417.0	204.213879	-0.452933	204.213879	-0.452933	23.8 ± 0.0	23.4 ± 0.0	23.3 ± 0.0	25.9 ± 0.9	1.4 ± 0.4	13.92	6.08	-0.02	2.95
borg_1408+5503.460.0	211.965695	55.052571	211.965695	55.052571	24.1 ± 0.0	23.7 ± 0.0	23.4 ± 0.0	25.7 ± 0.1	2.0 ± 0.8	16.44	19.45	15.97	-8.00
borg_1408+5503.557.0	211.951370	55.055894	211.951370	55.055894	23.1 ± 0.0	23.0 ± 0.0	23.0 ± 0.0	24.0 ± 0.0	0.7 ± 0.4	16.55	20.42	16.77	-8.83
borg_1408+5503.737.0	211.957313	55.059124	211.957313	55.059124	23.4 ± 0.0	23.2 ± 0.0	23.2 ± 0.0	24.1 ± 0.0	0.9 ± 0.1	16.79	22.79	18.71	-10.83
borg_1408+5503.920.0	211.977552	55.065975	211.977552	55.065975	23.9 ± 0.0	23.7 ± 0.0	23.6 ± 0.0	25.0 ± 0.1	-1.7 ± 0.3	16.98	24.87	20.41	-12.60
borg_1408+5503.932.0	212.010126	55.068508	212.010126	55.068507	23.2 ± 0.0	22.9 ± 0.0	22.6 ± 0.0	24.8 ± 0.1	-1.3 ± 0.1	15.67	13.64	11.21	-3.07
borg_1408+5503.977.0	211.965445	55.066386	211.965445	55.066386	23.9 ± 0.0	23.8 ± 0.0	23.7 ± 0.0	24.9 ± 0.1	-0.3 ± 0.4	17.32	29.09	23.88	-16.18
borg_1408+5503.1068.0	211.966709	55.064490	211.966709	55.064490	23.7 ± 0.0	23.3 ± 0.0	23.1 ± 0.0	25.2 ± 0.1	1.8 ± 0.2	16.09	16.51	13.56	-5.50
borg_1437+5043.83.0	219.225895	50.705228	219.225895	50.705228	22.9 ± 0.0	22.8 ± 0.0	22.5 ± 0.0	25.4 ± 0.2	-1.1 ± 0.1	13.33	4.63	3.61	4.91
borg_1437+5043.755.0	219.264083	50.723283	219.264083	50.723283	23.0 ± 0.0	22.7 ± 0.0	22.6 ± 0.0	26.2 ± 0.3	0.8 ± 0.6	11.52	2.01	1.58	6.94
borg_1437+5043.915.0	219.227427	50.735710	219.227427	50.735710	21.2 ± 0.0	21.0 ± 0.0	21.0 ± 0.0	24.3 ± 0.1	1.3 ± 0.2	10.06	1.03	0.82	7.70
borg_1437+5043.1010.0	219.249669	50.731502	219.249669	50.731502	22.2 ± 0.1	21.9 ± 0.0	21.9 ± 0.0	25.1 ± 0.1	-4.2 ± 0.1	10.97	1.57	1.24	7.29
borg_1524+0954.30.0	231.034060	9.886791	231.034060	9.886791	23.8 ± 0.1	23.6 ± 0.0	23.5 ± 0.1	26.1 ± 0.9	1.0 ± 0.1	15.29	11.43	1.99	1.31
borg_1524+0954.185.0	231.039430	9.894886	231.039430	9.894886	24.2 ± 0.0	23.8 ± 0.0	23.6 ± 0.0	26.1 ± 0.9	-1.0 ± 0.2	15.48	12.50	2.18	0.64
borg_1524+0954.189.0	231.043098	9.895765	231.043098	9.895765	22.8 ± 0.0	22.2 ± 0.0	21.9 ± 0.0	24.5 ± 0.9	1.1 ± 0.4	13.90	6.02	1.06	4.72
borg_1524+0954.487.0	231.057200	9.904472	231.057200	9.904472	24.2 ± 0.0	23.9 ± 0.0	23.7 ± 0.0	26.2 ± 0.9	-3.6 ± 0.1	15.59	13.13	2.29	0.25
borg_1524+0954.838.0	231.029652	9.915065	231.029652	9.915065	23.6 ± 0.0	23.3 ± 0.0	23.0 ± 0.0	25.6 ± 0.9	0.5 ± 0.1	14.92	9.62	1.68	2.45
borg_1555+1108.554.0	238.850119	11.130668	238.850119	11.130668	18.8 ± 0.0	18.3 ± 0.0	18.2 ± 0.0	21.9 ± 0.0	-1.3 ± 0.1	7.19	0.27	0.08	8.36
borg_1555+1108.557.0	238.843373	11.127897	238.843373	11.127897	24.3 ± 0.0	23.9 ± 0.0	23.9 ± 0.0	24.9 ± 0.1	-4.0 ± 0.1	17.42	30.49	-7.27	-2.27
borg_1555+1108.1235.0	238.853955	11.143454	238.853955	11.143454	24.1 ± 0.0	23.9 ± 0.0	23.8 ± 0.1	24.7 ± 0.1	2.5 ± 0.0	17.48	31.29	6.07	-7.68
borg_1632+3733.86.0	248.083466	37.542094	248.083466	37.542094	20.8 ± 0.0	20.5 ± 0.0	20.2 ± 0.0	22.9 ± 0.0	-5.4 ± 0.0	12.17	2.71	1.68	7.49
borg_1632+3733.266.0	248.093645	37.549245	248.093645	37.549245	20.5 ± 0.0	20.4 ± 0.0	20.3 ± 0.0	24.4 ± 0.1	1.1 ± 0.2	8.93	0.61	0.40	8.27
borg_1632+3733.492.0	248.073319	37.553174	248.073319	37.553174	24.5 ± 0.1	23.8 ± 0.1	23.5 ± 0.1	24.9 ± 0.1	0.3 ± 0.2	17.38	29.90	18.25	-2.66
borg_1632+3733.970.0	248.072548	37.571171	248.072548	37.571171	23.5 ± 0.0	23.4 ± 0.0	23.3 ± 0.0	24.8 ± 0.1	-3.2 ± 0.1	16.65	21.34	13.04	0.53
borg_1632+3733.1259.0	248.060575	37.563181	248.060575	37.563181	23.5 ± 0.0	23.4 ± 0.0	23.3 ± 0.0	24.5 ± 0.1	7.8 ± 0.7	16.93	24.32	14.86	-0.59
borg_1632+3733.1291.0	248.050008	37.560553	248.050008	37.560553	24.0 ± 0.0	23.8 ± 0.0	23.7 ± 0.0	25.6 ± 0.1	0.7 ± 0.1	16.80	22.96	14.02	-0.08
borg_1632+3733.1304.0	248.046027	37.561192	248.046027	37.561192	23.8 ± 0.0	23.5 ± 0.2	23.5 ± 0.0	24.3 ± 0.0	1.6 ± 0.1	17.08	26.06	15.91	-1.24
borg_1632+3737.280.0	247.875561	37.601900	247.875561	37.601900	23.8 ± 0.0	23.6 ± 0.1	23.7 ± 0.1	26.2 ± 0.9	2.6 ± 0.7	14.35	7.40	-5.13	13.67
borg_1632+3737.439.0	247.888489	37.606823	247.888489	37.606823	23.3 ± 0.0	23.1 ± 0.0	22.9 ± 0.0	25.4 ± 0.9	1.8 ± 0.2	14.79	9.07	-6.30	14.84
borg_2057+4412.119.0	314.337373	-44.219836	314.337373	-44.219836	24.1 ± 0.0	23.9 ± 0.0	23.8 ± 0.1	26.3 ± 0.9	1.4 ± 0.1	14.44	7.74	-5.37	13.91
borg_2057+4412.222.0	314.351217	-44.213663	314.351217	-44.213663	22.1 ± 0.0	21.8 ± 0.0	21.5 ± 0.0	24.0 ± 0.9	2.3 ± 0.2	13.41	4.81	-3.33	11.86
borg_2057+4412.345.0	314.333154	-44.210865	314.333154	-44.210865	23.8 ± 0.0	23.6 ± 0.1	23.7 ± 0.1	26.2 ± 0.9	2.6 ± 0.7	14.35	7.40	-5.13	13.67
borg_2057+4412.389.0	314.315098	-44.209357	314.315098	-44.209357	23.3 ± 0.0	23.0 ± 0.0	22.8 ± 0.0	24.8 ± 8.0	0.1 ± 0.3	17.11	26.37	16.12	-1.43
borg_2057+4412.473.0	314.313670	-44.206428	314.313670	-44.206428	23.3 ± 0.0	23.1 ± 0.0	22.9 ± 0.0	25.4 ± 0.9	1.9 ± 0.2	14.74	8.87	-6.16	14.70
borg_2057+4412.500.0	314.335035	-44.205529	314.335035	-44.205529	23.2 ± 0.0	22.9 ± 0.0	22.9 ± 0.0	25.5 ± 0.9	1.9 ± 0.3	13.46	4.93	-3.41	11.94
borg_2057+4412.698.0	314.321323	-44.199526	314.321323	-44.199526	24.2 ± 0.0	23.8 ± 0.1	23.8 ± 0.1	26.3 ± 0.9	0.3 ± 0.3	14.39	7.56	-5.24	13.78
borg_2132+1004.649.0	323.066868	10.082622	323.066868	10.082622	24.1 ± 0.1	23.8 ± 0.0	23.7 ± 0.1	26.2 ± 1.0	0.2 ± 0.0	14.33	7.36	1.32	14.38
borg_2132+1004.1021.0	323.071939	10.072133	323.071939	10.072133	23.7 ± 0.0	23.4 ± 0.0	23.2 ± 0.1	25.7 ± 0.9	-0.3 ± 0.1	15.11	10.50	1.86	16.89
borg_2132+1004.1052.0	323.057628	10.084320	323.057628	10.084320	24.2 ± 0.1	23.9 ± 0.0	23.9 ± 0.1	26.4 ± 1.0	2.6 ± 0.2	14.47	7.84	1.40	14.77
borg_2155+4411.1007.0	328.809295	-44.164652	328.809295	-44.164652	24.2 ± 0.0	24.0 ± 0.0	24.0 ± 0.1	26.5 ± 0.9	-0.9 ± 0.2	14.55	8.11	-5.62	15.44
borg_2155+4411.1162.0	328.840576	-44.172033	328.840576	-44.172033	23.7 ± 0.1	23.5 ± 0.0	23.3 ± 0.0	25.9 ± 0.9	0.2 ± 0.3	15.19	10.92	-7.59	17.85
borg_2203+1851.1056.0	330.700256	18.857744	330.700256	18.857744	23.4 ± 0.0	23.0 ± 0.0	22.9 ± 0.0	25.4 ± 0.9	-0.1 ± 0.3	14.71	8.74	2.85	16.12
borg_2345+0054.1412.0	356.275794	-0.898571	356.275794	-0.898571	24.0 ± 0.4	23.6 ± 0.0	23.5 ± 0.1	26.1 ± 0.9	-0.4 ± 0.2	15.31	11.52	-0.15	20.00
borg_2351+4332.89.0	357.658631	-43.541746	357.658631	-43.541746	23.5 ± 0.0	23.2 ± 0.0	23.0 ± 0.0	25.6 ± 0.9	1.5 ± 0.0	14.87	9.42	-6.46	17.92
borg_2351+4332.175.0	357.673299	-43.539723	357.673299	-43.539723	23.9 ± 0.0	23.6 ± 0.0	23.5 ± 0.0	26.0 ± 0.9	-3.0 ± 0.0	15.31	11.52	-7.91	20.01
borg_2351+4332.191.0	357.662943	-43.539585	357.662943	-43.539585	23.4 ± 0.0	23.0 ± 0.0	22.8 ± 0.0	26.3 ± 0.9	0.2 ± 0.3	14.67	8.59	-5.89	17.08
borg_2351+4332.442.0	357.658834	-43.533414	357.658834	-43.533414	23.9 ± 0.0	23.4 ± 0.0	23.5 ± 0.0	26.0 ± 0.9	0.3 ± 0.1	13.98	6.26	-4.28	14.75
borg_2351+4332.520.0	357.666248	-43.531533	357.666248	-43.531533	23.8 ± 0.0	23.6 ± 0.0	23.4 ± 0.0	26.0 ± 0.9	1.2 ± 0.4	15.23	11.11	-7.92	19.60
borg_2351+4332.734.0	357.671195	-43.523853	357.671195	-43.523853	24.5 ± 0.1	23.9 ± 0.0	23.7 ± 0.0	26.2 ± 0.9	0.2 ± 0.1	15.59	13.09	-8.99	21.58
borg_2351+4332.762.0	357.627558	-43.523279	357.627558	-43.523279	24.2 ± 0.0	23.9 ± 0.0	23.9 ± 0.0	26.5 ± 0.9	0.6 ± 0.2	14.46	7.79	-5.34	16.28
borg_2351+4332.1068.0	357.656164	-43.508214	357.656164	-43.508214	21.7 ± 0.0	21.3 ± 0.0	21.1 ± 0.0	23.7 ± 0.9	9.3 ± 0.1	12.93	3.86	-2.63	12.36



Table 14  
 – continued BORG13 M-dwarf identifications.

ID	ra	dec	l	b	$m_{F098M}$	$m_{F125W}$	$m_{F125W}$	$m_{F125W}$	$m_{F606W}$	Mtype	modulus	dist	Height	Radius
borg_0456-2203.156.0	73.972856	-22.064392	73.972856	-22.064392	24.2 ± 0.0	24.0 ± 0.0	23.9 ± 0.0	24.9 ± 0.0	-7.2 ± 0.0	-7.2 ± 0.0	17.51	31.81	-11.92	17.28
borg_0456-2203.438.0	73.973910	-22.057232	73.973910	-22.057232	23.1 ± 0.0	22.7 ± 0.1	22.4 ± 0.0	24.8 ± 0.1	-1.2 ± 0.2	-1.2 ± 0.2	14.33	7.35	-2.73	10.53
borg_0456-2203.706.0	73.954816	-22.052876	73.954816	-22.052876	23.6 ± 0.0	23.5 ± 0.0	23.4 ± 0.0	24.6 ± 0.0	1.9 ± 0.3	1.9 ± 0.3	17.08	26.06	-9.76	15.70
borg_0456-2203.1079.0	73.948592	-22.047464	73.948592	-22.047464	24.0 ± 0.4	23.8 ± 0.0	23.8 ± 0.1	25.1 ± 0.1	0.1 ± 0.3	0.1 ± 0.3	17.06	25.82	-9.66	15.64
borg_0951+3304.480.0	147.700413	33.058744	147.700413	33.058744	24.0 ± 0.0	23.9 ± 0.0	23.8 ± 0.0	25.1 ± 0.1	0.1 ± 0.3	0.1 ± 0.3	17.41	30.39	16.60	-17.19
borg_0951+3304.951.0	147.692507	33.063393	147.692507	33.063393	24.6 ± 0.0	24.0 ± 0.0	23.8 ± 0.0	25.9 ± 0.2	2.0 ± 0.5	2.0 ± 0.5	16.72	22.11	12.09	-10.19
borg_1059+0519.1299.0	164.710292	5.306348	164.710292	5.306348	24.5 ± 0.1	23.9 ± 0.0	23.6 ± 0.0	25.0 ± 0.1	1.4 ± 0.3	1.4 ± 0.3	17.46	31.05	2.90	-21.45
borg_1358+4334.428.0	209.456876	43.551383	209.456876	43.551383	24.1 ± 0.0	23.8 ± 0.0	23.7 ± 0.0	24.7 ± 0.0	-6.1 ± 0.1	-6.1 ± 0.1	17.36	29.68	20.48	-17.34
borg_1459+7146.300.0	224.786723	71.750951	224.786723	71.750951	24.1 ± 0.0	23.9 ± 0.0	23.7 ± 0.0	25.8 ± 0.1	2.0 ± 0.1	2.0 ± 0.1	16.67	21.58	20.52	-6.82
borg_1459+7146.459.0	224.805543	71.753068	224.805543	71.753068	24.2 ± 0.0	23.9 ± 0.0	23.8 ± 0.0	25.6 ± 0.1	-0.1 ± 0.1	-0.1 ± 0.1	16.96	24.68	23.47	-9.01
borg_1459+7146.796.0	224.706287	71.759250	224.706287	71.759250	23.4 ± 0.1	23.1 ± 0.0	22.9 ± 0.0	24.7 ± 0.0	2.0 ± 0.1	2.0 ± 0.1	16.11	16.69	15.88	-3.36
borg_1459+7146.992.0	224.775020	71.762522	224.775020	71.762522	24.3 ± 0.0	23.9 ± 0.0	23.7 ± 0.0	25.1 ± 0.1	4.6 ± 0.0	4.6 ± 0.0	17.42	30.44	28.93	-13.11
borg_1459+7146.1746.0	224.699176	71.774227	224.699176	71.774227	23.3 ± 0.0	22.9 ± 0.0	22.9 ± 0.0	24.0 ± 0.0	0.9 ± 0.3	0.9 ± 0.3	16.42	19.21	18.28	-5.16
borg_1510+1115.55.0	227.535356	11.223008	227.535356	11.223008	24.5 ± 0.0	23.9 ± 0.0	23.6 ± 0.0	25.2 ± 0.0	2.2 ± 0.3	2.2 ± 0.3	17.50	31.56	6.17	-12.81
borg_1510+1115.1110.0	227.534639	11.257096	227.534639	11.257096	24.3 ± 0.0	23.9 ± 0.0	23.8 ± 0.0	24.8 ± 0.0	3.2 ± 0.1	3.2 ± 0.1	17.41	30.30	5.94	-11.96
borg_2132-1202.566.0	322.947234	-12.057235	322.947234	-12.057235	23.7 ± 0.0	23.2 ± 0.0	23.0 ± 0.0	24.0 ± 0.0	9.8 ± 1.9	9.8 ± 1.9	16.76	22.48	-4.67	26.44
borg_2132-1202.7376.0	322.968345	-12.033277	322.968345	-12.033277	22.3 ± 0.1	22.1 ± 0.0	21.9 ± 0.0	24.1 ± 0.0	0.8 ± 0.1	0.8 ± 0.1	14.91	9.57	-1.97	16.14
borg_2313-2243.452.0	348.230552	-22.737392	348.230552	-22.737392	21.2 ± 0.0	20.9 ± 0.0	20.8 ± 0.0	24.7 ± 0.0	1.0 ± 0.1	1.0 ± 0.1	9.52	0.80	-0.28	9.28
borg_2313-2243.512.0	348.237747	-22.737423	348.237747	-22.737423	22.9 ± 0.0	22.7 ± 0.0	22.7 ± 0.0	25.2 ± 0.1	9.9 ± 3.3	9.9 ± 3.3	13.27	4.51	-1.72	12.92
borg_2313-2243.2534.0	348.242462	-22.718495	348.242462	-22.718495	24.1 ± 0.0	23.9 ± 0.0	23.9 ± 0.0	25.2 ± 0.0	3.3 ± 0.0	3.3 ± 0.0	17.21	27.63	-10.64	35.55
borg_2313-2243.3469.0	348.226934	-22.708732	348.226934	-22.708732	23.9 ± 0.0	23.7 ± 0.0	23.6 ± 0.0	25.3 ± 0.1	0.6 ± 0.2	0.6 ± 0.2	16.77	22.58	-8.69	30.61
borg_2313-2243.3529.0	348.235346	-22.709444	348.235346	-22.709444	23.0 ± 0.0	22.8 ± 0.0	22.5 ± 0.0	25.4 ± 0.1	0.3 ± 0.3	0.3 ± 0.3	13.31	4.60	-1.75	13.00
borg_2313-2243.3654.0	348.239365	-22.706295	348.239365	-22.706295	23.7 ± 0.0	23.5 ± 0.2	23.4 ± 0.0	24.9 ± 0.0	-1.3 ± 0.2	-1.3 ± 0.2	16.75	22.35	-8.60	30.38

**Table 15**  
The 1 T-dwarfs identified in BoRG.

ID	ra	dec	l	b	$m_{F098M}$	$m_{F125W}$	$m_{F125W}$	$m_{F125W}$	$m_{F606W}$
borg_0540-6409.1929.0	84.862502	-64.152446	84.862502	-64.152446	$22.9 \pm 0.0$	$21.9 \pm 0.0$	$22.2 \pm 0.0$	$21.5 \pm 0.0$	

**Table 16**  
The 30 L-dwarfs identified in BoRG.

ID	ra	dec	l	b	$m_{F098M}$	$m_{F125W}$	$m_{F125W}$	$m_{F125W}$	$m_{F606W}$
borg_0110-0224.1010.0	17.537240	-2.409470	17.537240	-2.409470	24.7 ± 0.1	23.7 ± 0.0	23.5 ± 0.0	23.5 ± 0.0	25.3 ± 0.1
borg_0439-5317.882.0	69.836642	-53.263207	69.836642	-53.263207	24.0 ± 0.0	22.7 ± 0.0	22.2 ± 0.0	22.2 ± 0.0	24.8 ± 0.9
borg_0540-6409.2993.0	84.876906	-64.132531	84.876906	-64.132531	25.0 ± 0.1	23.8 ± 0.0	23.4 ± 0.0	23.4 ± 0.0	26.8 ± 0.6
borg_0751-2917.567.0	117.684321	29.285619	117.684321	29.285619	19.5 ± 0.0	17.8 ± 0.0	17.6 ± 0.0	17.6 ± 0.0	19.6 ± 0.0
borg_0808-3946.457.0	122.094091	39.759095	122.094091	39.759095	25.0 ± 0.1	23.9 ± 0.0	23.5 ± 0.0	23.5 ± 0.0	26.9 ± 0.6
borg_0819-4911.264.0	124.831743	49.175806	124.831743	49.175806	23.9 ± 0.0	22.8 ± 0.0	22.4 ± 0.0	22.4 ± 0.0	27.9 ± 1.6
borg_0906-0255.462.0	136.409407	2.923645	136.409407	2.923645	24.4 ± 0.0	23.3 ± 0.0	22.8 ± 0.0	22.8 ± 0.0	27.6 ± 0.8
borg_0909-0002.748.0	137.292821	-0.012257	137.292821	-0.012257	24.5 ± 0.1	23.2 ± 0.0	22.8 ± 0.3	22.8 ± 0.3	26.6 ± 0.4
borg_0914-2822.673.0	138.558022	28.364206	138.558022	28.364206	24.8 ± 0.1	23.5 ± 0.0	23.1 ± 0.0	23.1 ± 0.0	26.3 ± 0.3
borg_0926-4426.581.0	141.355847	44.425445	141.355847	44.425445	24.3 ± 0.0	23.1 ± 0.0	22.6 ± 0.0	22.6 ± 0.0	25.2 ± 0.9
borg_1103-2330.623.0	165.819910	-23.506010	165.819910	-23.506010	23.9 ± 0.1	22.9 ± 0.0	22.5 ± 0.0	22.5 ± 0.0	25.7 ± 0.2
borg_1111-5545.1125.0	167.747157	55.771759	167.747157	55.771759	23.6 ± 0.0	22.5 ± 0.0	22.1 ± 0.0	22.1 ± 0.0	26.6 ± 0.3
borg_1153-0056.247.0	178.200215	0.922794	178.200215	0.922794	23.9 ± 0.0	22.9 ± 0.0	22.4 ± 0.0	22.4 ± 0.0	26.2 ± 0.3
borg_1230-0750.2419.0	187.471709	7.820117	187.471709	7.820117	23.9 ± 0.1	22.8 ± 0.0	22.3 ± 0.0	22.3 ± 0.0	26.2 ± 0.3
borg_1301-0000.1067.0	195.326828	0.013297	195.326828	0.013297	23.5 ± 0.1	22.2 ± 0.0	21.8 ± 0.0	21.8 ± 0.0	24.3 ± 0.9
borg_1337-0028.1117.0	204.205278	-0.445870	204.205278	-0.445870	24.3 ± 0.2	23.1 ± 0.0	22.7 ± 0.0	22.7 ± 0.0	25.3 ± 0.9
borg_1524-0954.24.0	231.044740	9.885957	231.044740	9.885957	24.9 ± 0.1	23.0 ± 0.1	22.8 ± 0.1	22.8 ± 0.1	25.3 ± 1.0
borg_1632-3733.65.0	248.069017	37.540353	248.069017	37.540353	24.5 ± 0.0	23.3 ± 0.0	22.9 ± 0.0	22.9 ± 0.0	28.5 ± 2.1
borg_1632-3733.349.0	248.080963	37.550065	248.080963	37.550065	23.5 ± 0.0	22.4 ± 0.0	22.0 ± 0.1	22.0 ± 0.1	27.1 ± 1.4
borg_1632-3733.1325.0	248.076265	37.572819	248.076265	37.572819	24.3 ± 0.0	23.0 ± 0.1	22.5 ± 0.0	22.5 ± 0.0	26.7 ± 0.5
borg_2132-1004.284.0	323.058751	10.068991	323.058751	10.068991	16.8 ± 0.0	15.0 ± 0.0	14.7 ± 0.0	14.7 ± 0.0	17.2 ± 0.9
borg_2132-1004.332.0	323.060235	10.059801	323.060235	10.059801	21.2 ± 0.0	19.9 ± 0.0	19.7 ± 0.0	19.7 ± 0.0	22.2 ± 0.9
borg_2155-4411.227.0	328.831076	-44.185153	328.831076	-44.185153	23.5 ± 0.0	22.5 ± 0.0	22.2 ± 0.0	22.2 ± 0.0	24.8 ± 0.9
borg_2155-4411.974.0	328.809893	-44.164189	328.809893	-44.164189	24.3 ± 0.0	23.0 ± 0.0	22.5 ± 0.0	22.5 ± 0.0	25.1 ± 0.9
borg_2351-4332.1314.0	357.668728	-43.514053	357.668728	-43.514053	25.2 ± 0.1	23.9 ± 0.0	23.5 ± 0.0	23.5 ± 0.0	26.0 ± 0.9
borg_0456-2203.920.0	73.945566	-22.049396	73.945566	-22.049396	24.6 ± 0.1	23.4 ± 0.0	23.2 ± 0.0	23.2 ± 0.0	24.4 ± 0.0
borg_1059-0519.644.0	164.717943	5.301323	164.717943	5.301323	24.4 ± 0.0	23.1 ± 0.0	22.6 ± 0.0	22.6 ± 0.0	26.5 ± 0.3
borg_1118-1858.1915.0	169.392755	-18.972497	169.392755	-18.972497	24.8 ± 0.0	23.8 ± 0.0	23.3 ± 0.0	23.3 ± 0.0	26.1 ± 0.1
borg_1459-7146.1298.0	224.751450	71.780685	224.751450	71.780685	24.8 ± 0.2	23.5 ± 0.0	23.1 ± 0.0	23.1 ± 0.0	25.7 ± 0.1
borg_2132-1202.6461.0	322.941469	-12.021619	322.941469	-12.021619	24.6 ± 0.1	23.4 ± 0.0	23.0 ± 0.0	23.0 ± 0.0	26.5 ± 0.4